MDPI

Article

Impact of On-Board Hybrid Energy Storage Devices on Energy-Saving Operation for Electric Trains in DC Railway Systems

Bolun Zhang [1], **Shaofeng Lu** [1,*] , **Yang Peng** [1], **Chaoxian Wu** [2] , **Guangzhao Meng** [1], **Minling Feng** [1] **and Bingjian Liu** [3]

1   Shien-Ming Wu School of Intelligent Engineering, South China University of Technology, Guangzhou 510000, China
2   School of Systems Science and Engineering, Sun Yat-sen University, Guangzhou 510000, China
3   Department of Mechanical, Materials and Manufacturing Engineering, University of Nottingham, Ningbo 315000, China
*   Correspondence: lushaofeng@scut.edu.cn

Abstract: To improve the energy-efficiency of transport systems, it is necessary to investigate electric trains with on-board hybrid energy storage devices (HESDs), which are applied to assist the traction and recover the regenerative energy. In this paper, a time-based mixed-integer linear programming (MILP) model is proposed to obtain the energy-saving operation for electric trains with different constraints of on-board HESDs, such as their capacity, initial state of charge (SOC), and level of degradation. The proposed integrated power flow model based on the train longitudinal dynamics, power split of on-board HESDs, and line impedance is discretized and linearized, aiming to minimize the net energy consumption (NEC). The results reveal that on-board HESDs with a higher capacity does not necessarily lead to a higher energy-saving rate; a lower or excessive initial SOC could undermine the energy-saving potential; considering the long-term train operation, the degradation of the Li-ion battery will influence the energy-saving operation for electric trains, as well as result in an energy-saving rate that ranges from 41.57% to 31.90%. The practical data from Guangzhou Metro Line 7 were applied in the simulations, which enhanced the practicality and effectiveness of the proposed method.

Keywords: energy-saving operation; on-board hybrid energy storage devices (HESDs); time-based mixed integer linear programming (MILP); rail transportation; net energy consumption (NEC)

1. Introduction

With the ever-increasing prices of energy and fossil fuels such as gasoline, electrified rail traffic is becoming one of the most common public transportation options for urban residents [1]. In China, Beijing, Shanghai, and Guangzhou, metro loads accounted for from 1.5% to 2.5% of the city's total load, which had become the largest single electricity load in the cities [2]. To cope with the increasing energy consumption problem of the urban rail transit system, the energy-saving operation for electric trains has become a hot topic. At present, on-board hybrid energy storage devices (HESDs) were utilized in some modern railway systems, which can supply traction energy and recover regenerative energy to improve the systems' energy efficiency [3,4].

As an emerging technology, on-board HESDs are usually composed of different types of energy storage devices, namely, batteries (BATs), supercapacitors (SCs), and flywheels, where the hybridization solutions to BATs and SCs are widely applied in electric vehicles and rail transportation [5,6]. BATs are well known for their high-energy density and large energy-storage abilities, which are often used to absorb regenerative braking energy [7]. However, BATs are generally bulky and can withstand a limited lifespan in the driving

range of electric trains. Li-ion BATs-driven light rail has been applied in the West Japan railway [8] and Ni-MH BATs-driven was installed in France tramway [9]. Alternatively, SCs can achieve a high number of cycle lifetime, such as 80,000 to 100,000 cycles, as well as providing instantaneous high power during traction operation, but face many practical problems associated with their low energy density and relatively higher economic cost [10]. The simplistic and novel hydrothermal approaches were reported to enhance the electrochemical activity of SCs, and all these results indicate a superb cycling performance after 4000 cycles [11–13]. In some urban rail transit systems, e.g., the Hong Kong and Warsaw metro systems, the SCs systems were applied, which can store an amount of energy ranging from 2.8 MJ to 45 MJ [14]. In addition, flywheels feature a higher stored energy density and a greater life span, while complicated mechanical containment systems and irregular vibration hamper energy efficiency [15]. The application scenario of flywheel energy storage was also mainly concentrated in heavy haul locomotives [16]. Based on the abovementioned discussion, adding on-board HESDs to form hybrid powertrain trains could improve the responsiveness of the power source to abrupt load changes during train traction operations and meet the peak power demand. However, the application of on-board HESDs consisting of Li-ion BATs and SCs based on the complementary features of the energy sources remains to be further explored.

The train operation consists of four typical movement modes [17]: (1) motoring mode, (2) cruising mode, (3) coasting mode, and (4) braking mode. During motoring and cruising operation, the train overcomes the drag resistance or the force due to its gradient and consumes the traction energy from the traction substations (TSSs) and on-board HESDs. In the coasting mode, the train is only affected by the drag resistance or the force due to the gradient. Braking efforts are then applied to reduce the train speed and the regenerative braking energy could be recycled by on-board HESDs in the braking operation. The energy-saving operation for electric trains could result in the minimum energy consumption as well as the optimal train speed profile within a given allowable error under the power split of on-board HESDs and train dynamics constraints [18].

In recent years, some studies considering both the on-board energy storage devices and the energy-saving operation for electric trains have become increasingly popular. Zhang et al. [19] introduced the Mixed Integer Linear Programming (MILP) model to optimize the speed profile and the capacity configuration for on-board HESDs, which focused on minimum economic costs considering the long-term train operation. In [20], the authors showed that the capacity of SCs and speed trajectory for Fuel-cell hybrid trains could be co-optimized to achieve minimum net hydrogen consumption. The distance-based model was proposed to obtain the speed trajectory and capacity solution with energy flow constraints [21]. By considering the capacity constraints of on-board HESDs, a rule-based energy management strategy was tested in CRRC Qingdao Sifang Co. Ltd, which aimed to improve train operation and optimize hydrogen consumption [22]. Moreover, many researchers derived some highly nonlinear State of Charge (SOC) models for energy storage devices and revealed the working mechanism between them and train operation through numerous experimental studies. In [23], a novel dynamic programming method was proposed to reveal the optimal operation control of trains with on-board Li-ion BATs. It concluded that the optimal train speed profile would depend on the SOC for Li-ion BATs, considering the track condition and speed limitations. A peak demand cutting strategy was applied to study the optimal energy-saving solution for the electric trains in the Thailand Silom Line, where the initial SOC of the on-board energy storage system had a huge effect on train operation [24]. Xia et al. [25] proposed an SOC-based energy management strategy, where the SCs could reduce the power dissipation of the train and voltage stress of the traction power grid. In [26], a coordinated optimal decision-making method based on train operation and on-board BATs was established, subject to the dynamic performance of the train and SOC. In most previous and proceeding papers, the train operation and power split of on-board HESDs were not jointly optimized, and the initial SOC and capacity were

only set as fixed parameters, which reduced the applicability of the model to electrified rail systems.

In addition to the important electrical parameters (SOC and capacity) of on-board HESDs, the degradation behavior of the BATs is also of considerable importance in the energy-saving operation of electric trains. Considering long-term train operation, the impact of the BATs' degradation on the energy-saving operations of electric trains could not be ignored due to its significant impact on the system's energy-saving performance. There are two common approaches to exploring the BATs' degradation: one is to build an electrochemical model, and the other is to develop a traditional empirical model [27]. Although the former could accurately predict actual degradation behavior within the BATs, it relied heavily on theory and was difficult to apply under practical conditions [28]. The latter required a large amount of data to fit the model parameters, but could not accurately represent the train operation and load profiles, since it was only valid under specific experimental conditions [29]. Zhang et al. [30] carried out a series of overcharge tests for ternary power BATs and evaluated the degradation characteristics of electrochemical models from microscopic perspectives. Li et al. [31] developed a novel deep learning algorithm to quantify the battery degradation phenomenon and explored the aging characteristics, where the estimation error was no greater than 3%. In [32], the authors analyzed the effect of complex vibration conditions on the degradation effect of Li-ion BATs during train operation. In [33], the authors selected different stress factors to explore the health feature of Li-ion BATs from a physics-based perspective. A hybrid estimation method based on incremental capacity and back-propagation neural network was proposed to accurately estimate of the state of health (SOH) of the Li-ion BATs [34]. The common features of the abovementioned works are that the majority were restricted to the applications of electric vehicles and the impact of BATs' degradation behavior on the energy-saving operation for electric trains was not fully considered.

The above review shows that the energy-saving operation for electric trains is discussed, while on-board HESDs are not involved or only a few properties of energy storage devices as fixed parameters are taken into account. Numerous studies have been conducted to evaluate the energy-saving potential of on-board energy storage devices, as summarized in Table 1. Although the integration of on-board HESDs in the traction system are considered to be an important and effective method for energy-saving operations, the energy-saving performance can be greatly affected by other factors. The mechanism is complicated and we need a complete integrative model to fully investigate and evaluate energy-saving performance. Based on the above discussion, this paper focuses on the problem of energy-saving operations for electric trains with on-board HESDs consisting of Li-ion BATs and SCs, while the properties of on-board HESDs (capacity, SOC, and degradation mechanisms) are introduced and investigated. The contributions of this article are outlined as follows.

(1) A novel time-based, mixed-integer, linear programming (MILP) model is developed, which could simplify and solve the derivative operations and the product operation of multiple time-varying parameters in complex nonlinear electrified rail transit systems by employing the proposed piecewise linearization (PWL) method. In some of the existing literature, the traction power systems are equivalent to infinite power sources [35] or the line impedance is neglected [26]. In this study, the proposed integration power flow model based on the train longitudinal dynamics, power split of on-board HESDs, and line impedance can further improve the accuracy of the system.

(2) This paper focuses on three important engineering characteristics of on-board HESDs (i.e., capacity, initial SOC, and degradation), further analyzes how these engineering characteristics affect the energy-saving operation of electric trains from the perspective of operations research, and reveals the intrinsic mechanism. The optimal energy-saving operation of electric trains under the different operating conditions of on-board HESDs can be located, where the corresponding train speed trajectory, power split of on-board HESDs and the solution of minimum net energy consumption (NEC) are all

obtained. The optimization results provide clear guidance for real-world engineering applications.

Table 1. Summary of the relevant studies on the modeling methods.

Publication	Objective/ Method	Consider SOC and Capacity	Consider Degradation Mechanism	Consider TSSs Model
Zhang et al. [19]	Minimum NEC/ MILP	Yes only optimized capacity	Yes	No
Meng et al. [20]	Minimum net hydrogen consumption/ MILP	Yes only optimized capacity	No	No
Sumpavakup et al. [24]	Maximize total saved energy/ Genetic algorithm	Yes only optimized SOC	No	Yes
Yang et al. [26]	Minimum cost / Mixed integer nonlinear programming	Yes only optimized SOC	No	No
Xiao et al. [36]	Minimum energy consumption/ Dynamic programming	Yes only optimized SOC	No	Yes
Wu et al. [35,37]	Minimum NEC/ MILP	Yes only optimized capacity	Yes	No
Kim et al. [38]	Minimum energy consumption/ Dynamic programming	Yes only optimized SOC	No	No
Zhang et al. (this work)	Minimum NEC/ MILP	Yes optimized	Yes	Yes

The remainder of this paper is organized as follows. Section 2 provides a detailed system setup of eanelectric train with on-board HESDs. In Section 3, the system model is elaborated, where the train longitudinal dynamics, on-board HESDs, the traction power system, energy flow modeling, constraints, and objective are shown. Section 4 covers the optimization results and a detailed discussion of different case studies. Finally, the conclusion is provided, along with a discussion of future work, in Section 5.

2. The System Setup of the Electric Train with On-Board HESDs

The schematic diagram of an electric train with on-board HESDs is shown in Figure 1. The system has the following components: Li-ion battery packs (MV06203127NTPCA, manufactured by Microvast Power), supercapacitor modules (BMOD0063-P125-B08, manufactured by Maxwell), DC-DC converters, and the traction motors associated with the braking resistors and non-reversible feeding substations. In the circuit topology, the electric train is supported by Li-ion BATs, SCs, and non-reversible feeding substations, where these energy sources are connected to the electric train load through DC-DC converters or DC bus.

Many researchers have found that the use of on-board HESDs allows for a more flexible system, where SCs and Li-ion BATs can improve the power density and energy density of the integrated system, respectively [19,39,40]. After considering the optimized scenarios and commonly used commercial components, the proposed integrated system in this work is mainly composed of: (1) each cell for Li-ion BATs is 10 Ah and 2.3 V. When the rated charge/discharge rate is 4 C, the rated charging power is -93.3 W and rated discharging power is 93.3 W [22]; (2) each module for BMOD0063-P125-B08 supercapacitor is 63 F, which is specifically designed for heavy transport applications such as electric trains, trolleys, cranes, etc. The electric energy is 0.14 kWh, and the rated power is 130 kW [41]; (3) the rated DC output voltage and power of the traction substation are 1500 V and 3 MW, respectively [36]. The main specifications of each system of the train are shown in Table 2. It should be noted that detailed models for power electronics and efficiency are not considered, that is, the power dissipated in DC-DC converters is not included in this study.
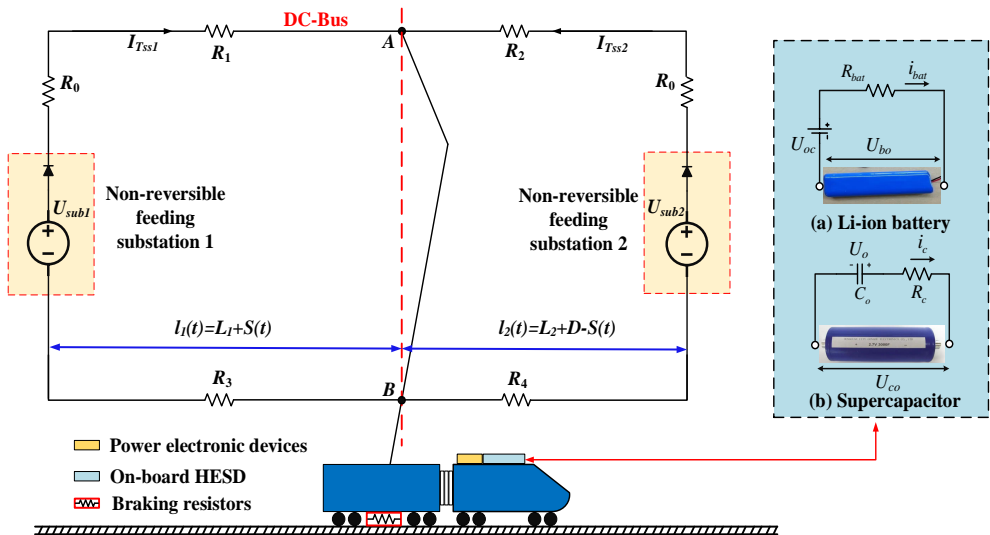
Figure 1. A schematic diagram for an electric train with on-board HESDs in DC traction supply network.

Table 2. Specifications of the on-board HESDs and TSSs for a typical electric train [22,36,41,42].

Component System	Parameter	Value
Li-ion BATs system	Model name	Microvast MV06203127NTPCA
	Cell capacity	10 Ah
	Rated power	−93.3 W (charge), 93.3 W (discharge)
	Cell voltage	1.86 V (min), 2.73 V (max), 2.3 V (rated)
	Electric energy	0.023 kWh
	Cell price	¥40
	Cell weight	0.3 kg
	Internal resistance	0.002 Ω
SCs system	Model name	Maxwell BMOD0063-P125-B08
	Module capacity	63 F
	Rated power	−130 kW (charge), 130 kW (discharge)
	Voltage	140 V (min), 225 V (max), 188 V (normal)
	Electric energy	0.14 kWh
	Module price	¥45,000
	Module weight	61 kg
	Equivalent DC series resistance	0.018 Ω
TSSs system	Substation DC voltage	1500 V
	Equivalent resistance R0	0.03 Ω
	Conductor rail resistivity coefficient ρ_1	0.014 Ω/km
	Running rail resistivity coefficient ρ_2	0.02 Ω/km

In addition, the scheme of non-reversible feeding substations means that the regenerative braking energy could not be transmitted back to the grid through the DC bus. Although it is interesting to integrate a reverse power flow into electric transportation systems to generate more efficient energy reuse solutions, its scalability, cost, and complexity due to the high coupling hinder further development [42]. In addition, the solution to reverse power flow has not been diffused because the troubles of multi-level energy source cooperative control need to be solved.

3. Optimization and System Modeling

In this section, the formulations of train longitudinal dynamics, DC traction power system, and on-board HESDs power flow based on the time-MILP approach are elaborated.

Although the researchers in our group have published some works on distance-based MILP models [19,35,37], which have been proved to have excellent robustness and fast optimization characteristics, heavy computational burdens are obtained when calculating the nonlinear constraints, especially the derivation of SOC for on-board HESDs and product operation of multiple time-varying parameters. Alternatively, as shown in Figure 2, the discretization process of the proposed, time-based MILP model is revealed, where each time segment Δt is a known parameter and the distance S_i ($i = 1, 2, 3 \ldots I$) are variables. After discretizing the travel time for the entire journey, the starting and ending speed data for each distance S_i ($i = 1, 2, 3 \ldots I$) can be collected. It should be noted that a shorter time segment Δt means that the optimization results are more accurate, but the computational time of the model will be longer.
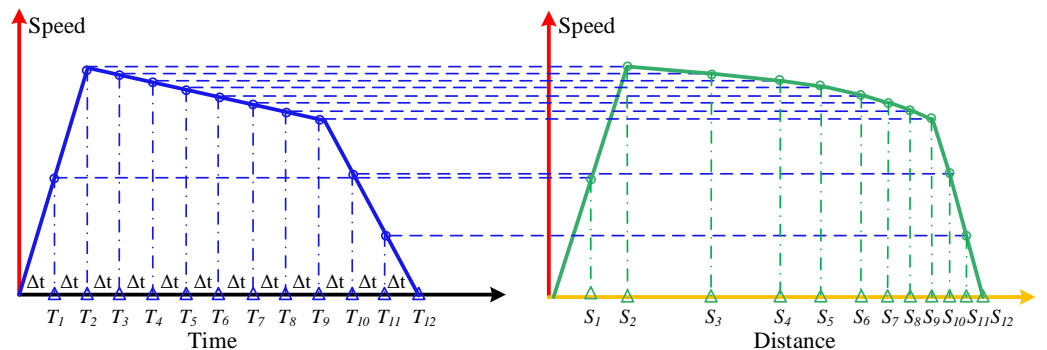
Figure 2. The discretization process of the interstation section is based on the proposed time-based MILP model. The blue and green solid lines are the train speed trajectory. The blue and green circles are the corresponding speed points in each time segment Δt and the blue dotted lines are discrete divisions mapped to distances.

3.1. Train Longitudinal Dynamics

The discretization process of the train operation is to simplify the calculation in the proposed time-based MILP model. The train journey time T_i for the ith section is composed of several interval time $\Delta t_{i,j}$ with different values. In the time-based MILP model, the journey time T_i should be discretized and divided into several time segments $\Delta t_{i,j}$, which can be expressed by (1):

$$\sum_{j=1}^{N_i} \Delta t_{i,j} = T_i, i = 1, 2, 3 \ldots I \tag{1}$$

where N_i is the total number of the divided time segments for T_i. Therefore, when the train travels in the journey time T_i, there are always $(N_i + 1)$ speed points in total, i.e., $V_{i,1}$, $V_{i,2}$, $\ldots$, V_{i,N_i+1}, and the average speed $V_{i,j,ave}$ in each $\Delta t_{i,j}$ can be calculated using the speed points, where $j = 1, 2, 3 \ldots N_i + 1$:

$$V_{i,j,ave} = \frac{V_{i,j} + V_{i,j+1}}{2}. \tag{2}$$

In each $\Delta t_{i,j}$, the corresponding interval distance $\Delta d_{i,j}$ can be calculated by the following equation:

$$\Delta d_{i,j} = V_{i,j,ave} \times \Delta t_{i,j} = \frac{V_{i,j} + V_{i,j+1}}{2} \times \Delta t_{i,j}. \tag{3}$$

In the model, the acceleration or deceleration values $a_{i,j}$ of the train are assumed to be unified in each time segment $\Delta t_{i,j}$. This can be obtained as shown in (4):

$$a_{\mathrm{d}max} \leq a_{i,j} = \frac{(V_{i,j+1} - V_{i,j})}{\Delta t_{i,j}} \leq a_{\mathrm{a}max} \tag{4}$$

where $a_{\mathrm{d}max}$ and $a_{\mathrm{a}max}$ represent maximum deceleration and maximum acceleration, respectively. When the train is operating on the track, the drag force $F_{i,j,dr}$ in each $\Delta t_{i,j}$ can be expressed by the Davis Equation, as shown in (5):

$$F_{i,j,dr} = A + BV_{i,j,ave} + CV_{i,j,ave}^2 \tag{5}$$

where A, B, and C are the Davis coefficients. During the journey, the upper boundary of train speed V_{max} should be limited due to real-world operation, and can be set as shown in (6):

$$V_{i,j} \leq V_{max}. \tag{6}$$

3.2. Modeling of On-Board HESDs System

Although many researchers have developed a Li-ion battery model based on electrochemical characteristics, which can accurately predict the voltage dynamics, its complex structure is not conducive to optimal modeling [43]. Concerning the complexity and accuracy of the Li-ion battery model, a mature equivalent circuit model with a single state is employed, which consists of open-circuit voltage U_{oc} and internal resistance R_{bat} in series, as shown in Figure 1 [38]. The dynamic electrical behavior can be captured by (7):

$$\begin{cases} U_{bo}(t) = U_{oc} - I_{bat}(t)R_{bat} \\ P_{bat}(t) = U_{oc}I_{bat}(t) - I_{bat}^2(t)R_{bat} \end{cases} \tag{7}$$

where $U_{bo}(t)$ and $I_{bat}(t)$ represent the terminal voltage and current of the Li-ion BATs; $P_{bat}(t)$ represents the output power. As a typical case in transportation planning problems, the capacity of on-board HESDs should be treated as a measure of electric charge. As a result, the SOC of on-board HESDs should refer to the current proportion of the stored electric charge inside with respect to the maximum possible charge that they can hold [27]. Typically, the current $I_{bat}(t)$ is related to $SOC_{bat}(t)$, which satisfies (8):

$$\Delta SOC_{bat}(t) = -\frac{I_{bat}(t)}{3600 \times Q_{bat}} \cdot \Delta t_{i,j} \tag{8}$$

where Q_{bat} is the Li-ion battery capacity in Ah, and $I_{bat}(t)$ is considered as negative during the charging operation. The $SOC_{bat}(t)$ and electrical characteristics are limited by the physical property of the Li-ion BATs, given as follows:

$$\begin{cases} SOC_{bat,min} \leq SOC_{bat}(t) \leq SOC_{bat,max} \\ U_{bat,min} \leq U_{bo}(t) \leq U_{bat,max} \\ P_{bat,min} \leq P_{bat}(t) \leq P_{bat,max} \end{cases} \tag{9}$$

where $SOC_{bat,max}$ and $SOC_{bat,min}$ are the upper and lower limit of the Li-ion BATs SOC; $U_{bat,max}$ and $U_{bat,min}$ are maximum and minimum voltage of the Li-ion BATs; $P_{bat,max}$ and $P_{bat,min}$ are maximum and minimum power of the Li-ion BATs.

The equivalent electrical model of the SCs is modelled as the standard RC circuit, which is composed of a capacitor C_o in series with a resistance R_c, as shown in Figure 1 [36]. The model mainly focuses on the electrical behavior of the SCs, which satisfies (10):

$$\begin{cases} U_{co}(t) = U_o - I_c(t)R_c \\ P_{sc}(t) = U_o I_c(t) - I_c^2(t)R_c \end{cases} \tag{10}$$

where $U_{co}(t)$, U_o, $I_c(t)$, and $P_{sc}(t)$ represent the terminal voltage of the SCs, the voltage of the equivalent serial capacitor C_o, actual current, and output power of the SCs, respectively. On the other hand, the definition of the supercapacitor $SOC_{sc}(t)$ is similar to the Li-ion battery model [22], which is given by:

$$\Delta SOC_{sc}(t) = -\frac{I_c(t)}{C_o(U_{sc,max} - U_{sc,min})} \cdot \Delta t_{i,j} \tag{11}$$

where $U_{sc,max}$ and $U_{sc,min}$ represent the allowed fully charged voltage and fully discharged voltage of the SCs, respectively. It is worth mentioning that the SOC recursive identification of the SCs is similar to the Li-ion BATs in the modeling process. Considering the limit of the SCs operation conditions, the constraints of the optimization are expressed as:

$$\begin{cases} SOC_{sc,min} \leq SOC_{sc}(t) \leq SOC_{sc,max} \\ U_{sc,min} \leq U_{co}(t) \leq U_{sc,max} \\ P_{sc,min} \leq P_{sc}(t) \leq P_{sc,max} \end{cases} \tag{12}$$

where $SOC_{sc,max}$ and $SOC_{sc,max}$ are the maximum and minimum allowable SOC values of the SCs; $P_{sc,max}$ and $P_{sc,min}$ are maximum and minimum allowable power values of the SCs. Note that, the operating range of the SOC for on-board HESDs is set from 30% to 90% to avoid being fully charged or fully discharged.

3.3. Modeling of Traction Power System

Concerning the network of the DC-electrified railway system, the equivalent circuit diagram of the traction power system is shown in Figure 3, where it mainly contains the TSSs, train, conductor rail, and running rail. To analyze the dynamic characters of the circuit, the contact line has been modelled as a series of variable resistance and their values depend on the distance between the train and the feeding TSSs within each line span [42].
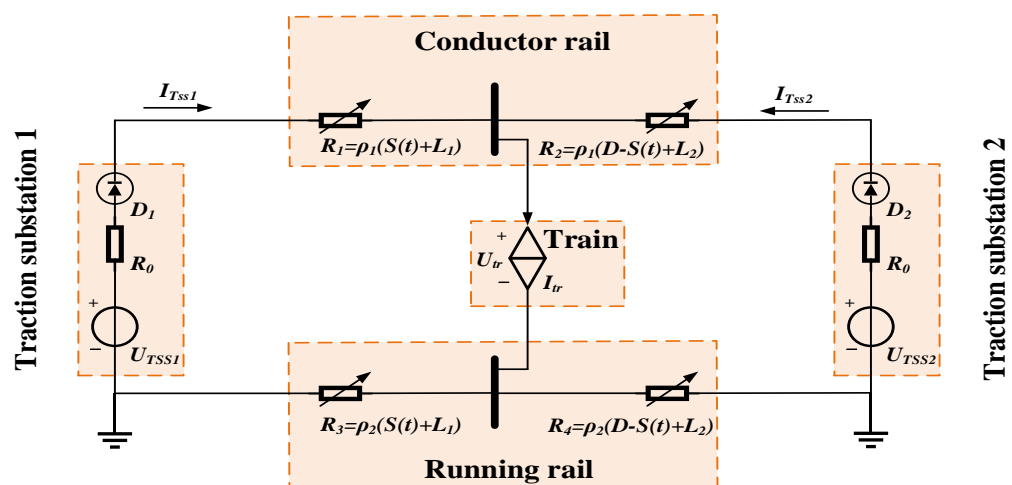

Figure 3. Equivalent circuit of DC traction power system.

In particular, the feeding TSSs have been modelled as a DC voltage source U_{Tss1} and U_{Tss2}, which are connected in series with lumped resistances R_0 and diodes, such that the

internal losses and the non-reversibility of the feeding TSSs are correctly considered. From Figure 3, the equivalent resistance can be calculated as:

$$\begin{cases} R_1(t) = \rho_1(S(t) + L_1) \\ R_2(t) = \rho_1(D - S(t) + L_2) \\ R_3(t) = \rho_2(S(t) + L_1) \\ R_4(t) = \rho_2(D - S(t) + L_2) \end{cases} \tag{13}$$

where D is the total distance from starting station to the terminal station; L_1 and L_2, respectively, represent the distance between adjacent non-reversible feeding TSSs and stations. According to the Kirchhoff Current Law, the output power of non-reversible feeding TSSs $P_{sub}(t)$ and the power received by the train $P_{tr}(t)$ are, respectively, expressed as:

$$\begin{cases} P_{\text{sub}}(t) = U_{\text{sub}} \left(\dfrac{U_{\text{sub}} - U_{tr}(t)}{R_0 + R_1(t) + R_3(t)} + \dfrac{U_{\text{sub}} - U_{tr}(t)}{R_0 + R_2(t) + R_4(t)} \right) \\ P_{tr}(t) = U_{tr}(t) \left(\dfrac{U_{\text{sub}} - U_{tr}(t)}{R_0 + R_1(t) + R_3(t)} + \dfrac{U_{sub} - U_{tr}(t)}{R_0 + R_2(t) + R_4(t)} \right) \end{cases} \tag{14}$$

where U_{sub} is substation DC voltage; $U_{tr}(t)$ is the voltage of the train from the catenary. In addition, the losses from the catenary E_{loss} can be calculated as:

$$E_{\text{loss}} = \sum_{j=1}^{N_i} (P_{sub}(t) - P_{tr}(t)) \times \Delta t_{i,j}, i = 1, 2, 3 \ldots \text{I}. \tag{15}$$

3.4. Energy Flow Modeling

The energy flow is transmitted between the energy supply side (non-reversible feeding TSSs or on-board HESDs) and the energy consumption side (train motor). In each $\Delta t_{i,j}$, when the train conducts traction or braking operations, it could either consume the energy from the feeding TSSs and on-board HESDs or regenerate the energy and then transfer it back to on-board HESDs. For each $\Delta t_{i,j}$, suppose $E_{i,j,t}$ is the traction energy and $E_{i,j,b}$ is the braking energy. It is worth noting that when the train motor consumes the energy from the feeding TSSs and on-board HESDs during traction, the discharge power of Li-ion BATs P_{batd} and SCs P_{scd} is greater than 0. Thus, according to the law of conservation of energy, traction energy $E_{i,j,t}$ satisfies:

$$E_{i,j,t} = P_{tr}(t) \times \Delta_{i,j} \times \eta_m + P_{batd}(t) \times \Delta t_{i,j} \times \eta_{bat} + P_{scd}(t) \times \Delta t_{i,j} \times \eta_{sc} \tag{16}$$

where η_m, η_{bat}, and η_{sc} are the average transmission efficiency of the motor, Li-ion BATs, and SCs, respectively. The braking energy $E_{i,j,b}$ is assumed to be equal to the sum of hydraulic braking energy $E_{i,j,hyd}$ and electric braking energy that could be recycled by on-board HESDs in each $\Delta t_{i,j}$. It is important to note that electric braking energy can only be fully charged by on-board HESDs or dissipated by the braking resistors in this study. The $E_{i,j,b}$ can be calculated:

$$E_{i,j,b} = \frac{P_{batc}(t) \times \Delta t_{i,j}}{\eta_{bat}} + \frac{P_{scc}(t) \times \Delta t_{i,j}}{\eta_{sc}} + E_{i,j,hyd} \tag{17}$$

where P_{batc} and P_{scc} are the charge power of the Li-ion BATs and SCs, respectively. Note that when the train conducts regenerative braking, $E_{i,j,b}$, P_{batc}, P_{scc}, and $E_{i,j,hyd}$ are both assumed to be negative quantities.

According to the law of conservation of energy, when the train conducts traction operation, $E_{i,j,t} \geq 0$, the energy from the non-reversible feeding TSSs and on-board HESDs is consumed by the train motor and transformed into kinetic energy, potential, and heat energy. Similarly, when the train implements braking operation, $E_{i,j,b} \leq 0$, the kinetic

energy is transformed into heat, potential energy, and electric energy that is fed back to on-board HESDs. Here, $E_{i,j,m}$ is the traction energy or the regenerative energy, and it holds that:

$$E_{i,j,m} - \frac{1}{2}(M_t + M_{HESDs})\left(V_{i,j}^2 - V_{i,j-1}^2\right) - F_{i,j,dr} \cdot \Delta d_{i,j} - (M_t + M_{HESDs})g\Delta h_{i,j} \geq 0 \quad (18)$$

where the mass of the train, the mass of the on-board HESDs, and height difference of the interval time are denoted as M_t, M_{HESDs}, $\Delta h_{i,j}$, respectively.

In addition to the energy conservation constraint, the train motors should conform to physical characteristic constraints. During traction or braking mode, the power of train motors should not exceed the maximum traction power $P_{t,max}$ or the maximum braking power $P_{b,max}$.

$$P_{tr}(t) \times \Delta t_{i,j} \cdot \eta_m + P_{batd}(t) \times \Delta t_{i,j} \cdot \eta_{bat} + P_{scd}(t) \times \Delta t_{i,j} \cdot \eta_{sc} \leq P_{t,max}\Delta t_{i,j}. \quad (19)$$

$$\frac{P_{batc}(t) \times \Delta t_{i,j}}{\eta_{bat}} + \frac{P_{scc}(t) \times \Delta t_{i,j}}{\eta_{sc}} \leq P_{b,\,max} \Delta t_{i,j}. \quad (20)$$

Furthermore, the work of the train motor must be restricted by the maximum traction force $F_{t,max}$ and the maximum braking force $F_{b,max}$. Thus, we have:

$$P_{tr}(t) \times \Delta t_{i,j} \cdot \eta_m + P_{batd}(t) \times \Delta t_{i,j} \cdot \eta_{bat} + P_{scd}(t) \times \Delta t_{i,j} \cdot \eta_{sc} \leq F_{t,\,max} \Delta d_{i,j}. \quad (21)$$

$$\frac{P_{batc}(t) \times \Delta t_{i,j}}{\eta_{bat}} + \frac{P_{scc}(t) \times \Delta t_{i,j}}{\eta_{sc}} \leq F_{b,max}\Delta d_{i,j}. \quad (22)$$

Binary variables λ_i are introduced to guarantee that the traction and braking operations will not occur simultaneously in real world, and are realized as follows:

$$E_{i,j,m} = \lambda_i E_{i,j,t} + (1 - \lambda_i)E_{i,j,b} \quad (23)$$

where λ_i is equal to 0 or 1. This means that when $\lambda_i = 1$, there is only discharge energy from on-board HESDs and the non-reversible feeding TSSs instead of the charge energy from on-board HESDs, and vice versa.

Moreover, the above variables are given by:

$$
\begin{cases}
0 \leq P_{tr}(t)\Delta t_{i,j} \cdot \eta_m \leq \lambda_i M_1 \\
0 \leq P_{batd}(t)\Delta t_{i,j} \cdot \eta_{bat} \leq \lambda_i M_1 \\
0 \leq P_{scd}(t)\Delta t_{i,j} \cdot \eta_{sc} \leq \lambda_i M_1 \\
0 \leq \dfrac{P_{batc}(t) \times \Delta t_{i,j}}{\eta_{bat}} \leq (1 - \lambda_i)M_2 \\
0 \leq \dfrac{P_{scc}(t) \times \Delta t_{i,j}}{\eta_{sc}} \leq (1 - \lambda_i)M_2 \\
0 \leq E_{i,j,hyd} \leq (1 - \lambda_i)M_2
\end{cases}
\quad (24)
$$

where M_1 and M_2 are two sufficiently large constants. Note that the main focus of this work is the optimization of electric train speed trajectory and power split of on-board HESDs and, hence, is concerned with power flows among powertrain components, i.e., the non-reversible feeding TSSs, the Li-ion BATs, the SCs, and the motor; therefore, detailed models of power electronics are not considered.

In short, the modeling approach is to discretize the total journey time, and then deal with nonlinear constraints by employing the PWL method (detailed in Appendix A). By

adopting the commercial available MILP solving algorithm, an optimal solution can be located within the feasible region of the model.

The objective of the proposed model is to minimize the total energy consumption during the journey, where the NEC value of the journey can be expressed as follows:

$$\sum_{i=1}^{I} E_i = \sum_{i=1}^{I} \sum_{j=1}^{N_i} (P_{sub}(t) + P_{batd}(t) + P_{scd}(t) + P_{batc}(t) + P_{scc}(t)) \times \Delta t_{i,j}. \tag{25}$$

By conducting the proposed time-based MILP model, we conducted the following optimization shown in (26):

$$Min: \quad \sum_{i=1}^{I} E_i \tag{26}$$

$$Subject \quad to: \quad (1) - (24), (A1) - (A12)$$

The proposed time-based MILP algorithm exploits the solution space to find a minimal NEC solution. As such, the model can efficiently determine the optimal train operation and power split of on-board HESDs, after considering the train longitudinal dynamics, on-board HESDs equivalent circuit model, and line impedance model.

4. Case Studies and Result Discussion

In this section, three scenarios corresponding to Sections 4.1–4.3 in the case studies are listed as follows:

- In Section 4.1, we aimed to reveal the impact of the different capacity of on-board HESDs on the train operation, where case 1 is assumed to be unequipped with on-board HESDs as a comparison. Here, for the sake of compactness, cases 2–3 are selected, where the parameters can be easily modified in the model. The optimal energy-saving operation for electric trains and power split for on-board HESDs are only displayed when the capacity is changed under capital cost constraints.

- Based on the optimization results in Section 4.1, we aimed to reveal the impact of the different initial SOC on the train operation and further explore the energy-saving potential of on-board HESDs. Similarly, three typical initial SOC values are selected in cases 4–6, which correspond to the minimum allowable value, the middle value, and the maximum allowable value, respectively.

- Based on the optimization results in Sections 4.1 and 4.2, on-board HESDs with optimal capacity and initial SOC were selected to reveal the impact of degradation on train operation. Cases 7 and 8 correspond to fresh and end-of-life cells, respectively, which fully demonstrate the significant differences in optimal train operation and power split strategies under different states of health.

The different cases for on-board HESDs configuration scenarios were discussed using a real route based on the data from the Guangzhou Metro Line 7. The route covers 3028 m, two feeding electricity TSSs, and three stations, where the route structure is shown in Figure 4. The main parameters were tabulated in Table 3. The mass of the train for AW2 in Guangzhou metro line 7 is 279.1 tons without on-board HESDs, and the maximum operational speed cannot exceed 80 km/h. The maximum acceleration $a_{a,max}$ and deceleration $a_{d,max}$ are both set at 1 m/s^2.
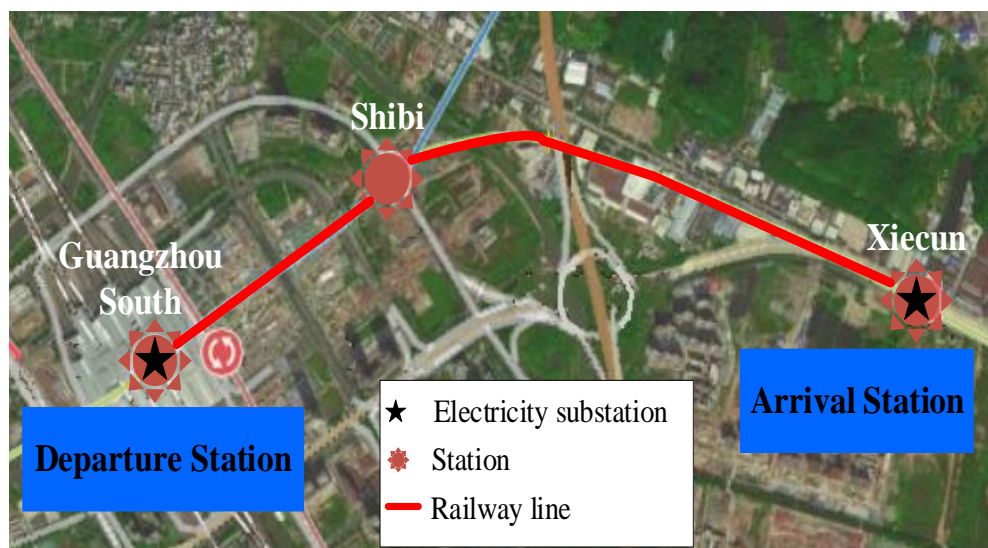
Figure 4. The part of route structure in Guangzhou metro line 7 from Google map.

Table 3. Key parameters in Guangzhou metro line 7 for a typical railway vehicle with on-board HESDs [17,19,44,45].

Symbol	Description	Value/Equation
M_t, (tonnes)	The total mass of the train	279.1 (AW2)
V_max, (km/h)	Maximum operational speed	80
$a_{a,max}$, (m/s^2)	Maximum acceleration	1.0
$a_{d,max}$, (m/s^2)	Maximum deceleration	1.0
η_m	Motor efficiency	90%
η_{bat}	Li-ion BATs efficiency	90%
η_{sc}	SCs efficiency	90%
$F_{t,max}$, (kN)	Maximum Tractive effort	289
$F_{b,max}$, (kN)	Maximum Braking effort	352
$P_{t,max}$, (kW)	Maximum traction power	3716
$P_{b,max}$, (kW)	Maximum braking power	3911
$F_{i,j,dr}$, (N/tonnes)	Resistance	$27 + 0.0042v^2$
$\Delta t_{i,j}$, (s)	interval time	2
T, (s)	Total journey time	220
D, (m)	Total travel distance	3028
$SOC_{bat,max}$	Maximum BATs SOC	90%
$SOC_{bat,min}$	Minimum BATs SOC	30%
$SOC_{sc,max}$	Maximum SCs SOC	90%
$SOC_{sc,min}$	Minimum SCs SOC	30%

The average energy efficiency of on-board HESDs η_{bat} and η_{sc} is set to be 0.9 considering negligible transmission loss [19]. In [44,45], the efficiency of the advanced DC and induction motors are about 90–94% and 93–95%, respectively, and then approximately set as 90%. By exploring the model, $\Delta t_{i,j} = 2s$ is shown to provide a better compromise between computational burden and accuracy. As mentioned in [17], the maximum traction power and braking power are obtained in the field test, as well as maximum tractive effort and braking effort. All of these parameter values in Table 3 can be modified according to the field data collected from different types of traction power systems and on-board HESDs. This paper presents a simulation where the used parameters are provided by the Guangzhou metro line 7 for journeys from Guangzhou South Station to Xiecun Station. Table 4 shows the scheduled information of railway vehicles.

Table 4. Scheduled information of railway vehicle [17].

	Stations	Distance between Stations (m)	Journey Time (s)
1	Guangzhou South → Shibi	1120	90
2	Shibi → Xiecun	1908	130
	Total	3028	220

4.1. Impact of Different On-Board HESDs Capacity on Train Operation Under Capital Cost Constraints

In this subsection, the influence of different on-board HESDs capacities on power split and train operation under capital cost constraints is investigated. As a comparison, the capacity of on-board HESDs in Case 1 is assumed to be 0 MJ, to indicate that the train is not equipped with on-board HESDs. Concerning cases 2 and 3, the specific capacity configuration of on-board HESDs and optimization results are shown in Table 5. The initial SOC for the on-board HESDs is 50% for cases 2 and 3, which can be modified in the model.

Table 5. The specific parameter and optimization results for cases 1–3.

Case	1	2	3
Li-ion BATs maximum power (kW)	0	209.9	419.8
Li-ion BATs electric energy (kWh)	0	51.75	103.5
No. of Li-ion BATs	0	225 (in series) × 10 (in parallel)	225 (in series) × 20 (in parallel)
Pack capacity (Ah)	0	100	200
Capital cost (¥)	0	90,000	180,000
SCs maximum power (kW)	0	260	520
SCs electric energy (kWh)	0	0.28	0.56
No. of SCs	0	2 (in series)	2 (in series) × 2 (in parallel)
Module capacity (F)	0	31.5	63
Capital cost (¥)	0	90,000	180,000
NEC (MJ)	74.63	60.54	52.07

As shown in Figures 5 and 6, the optimal operation of the train and power split show substantial differences when the capacity and power of on-board HESDs are different in cases 1–3. From Figure 5, when the railway vehicle operates without on-board HESDs in case 1, this means that the trains cannot recover and reuse regenerative braking energy through electrical braking. It should be noted that the train operation conforms to the law of conservation of energy, and when the output power is less than 0, this means that the on-board HESDs are in the charging state. In Figure 6, it can be observed that the propulsion energy of the train mainly comes from the non-reversible feeding TSSs and discharge energy from on-board HESDs during traction operation. Subsequently, the potential energy of the train caused by height differences can be converted into kinetic energy, on-board HESDs energy, and heat energy. During the train's braking operations, the kinetic energy can be converted into electrical energy, which can be recovered by the on-board HESDs. In addition, it is evident that the charge/discharge rate of SCs is significantly faster than that of Li-ion BATs due to their respective characteristics. The SCs are discharged to a minimum SOC value, i.e., 30% during traction operation, and charged to a maximum SOC value, i.e., 90% during braking operation, while the SOC of the Li-ion BATs slowly changes throughout the journey.
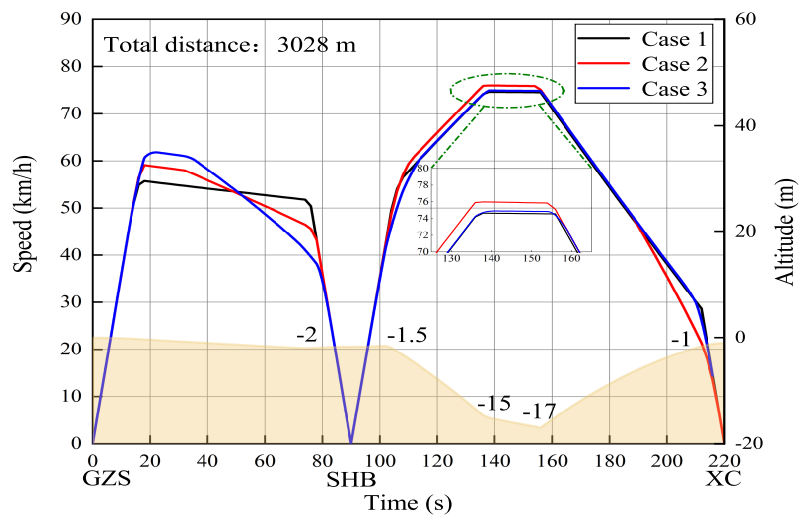
**Figure 5.** The optimal speed trajectories and altitude profile for cases 1–3.

(**a**)

(**b**)
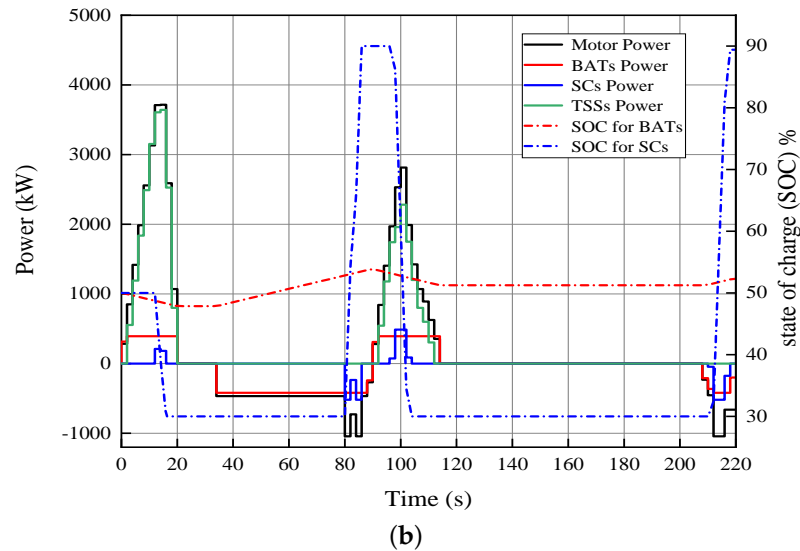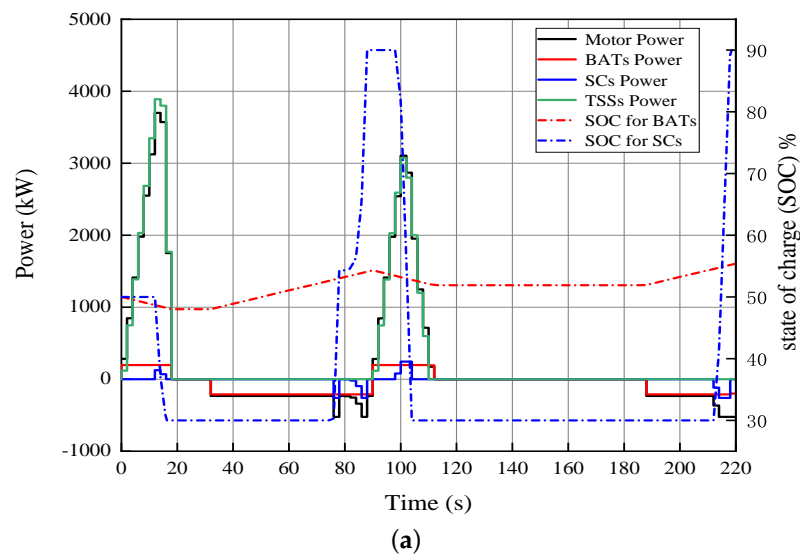
Figure 6. The motor power, TSSs power, discharge/charge power of on-board HESDs and SOC curves for cases 2–3. (**a**) case 2. (**b**) case 3.

As shown in Figures 6 and 7, the energy consumption and peak power of the feeding TSSs in case 3 are lower than that in case 2, and the on-board HESDs in case 3 can recover and reuse more braking energy, which results in a minimal NEC solution in case 3.
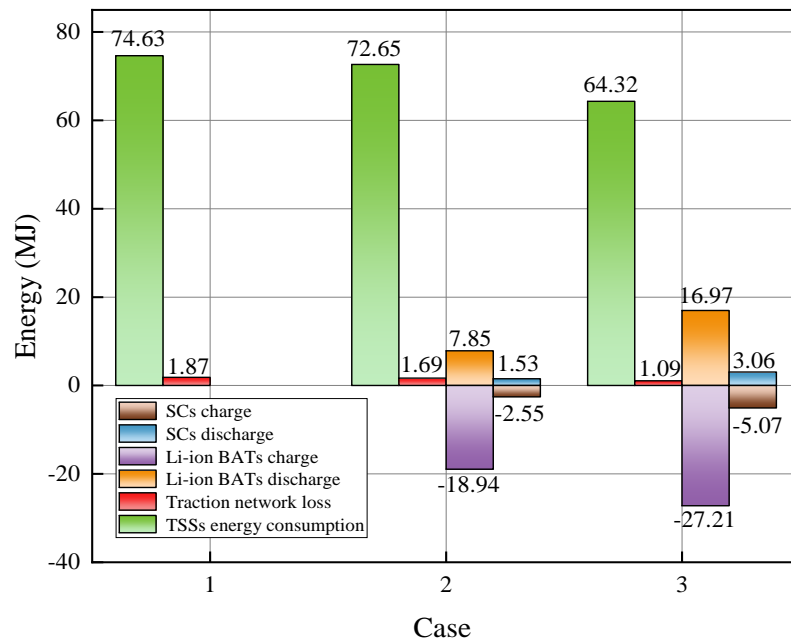

Figure 7. The energy flow of all the components in cases 1–3.

The relationship between the NEC and different maximum power of on-board HESDs under varying capital cost constraints is illustrated in Figure 8. Figure 8 shows that, with the increase in the maximum power and capacity of on-board HESDs, the solutions of NEC first drop quickly and then slightly increase. When the maximum power of the Li-ion BATs and the SCs is 1049.6 kW and 1560 kW, respectively, the proposed model obtains the optimization solution and the minimum NEC, which is 44.01 MJ.
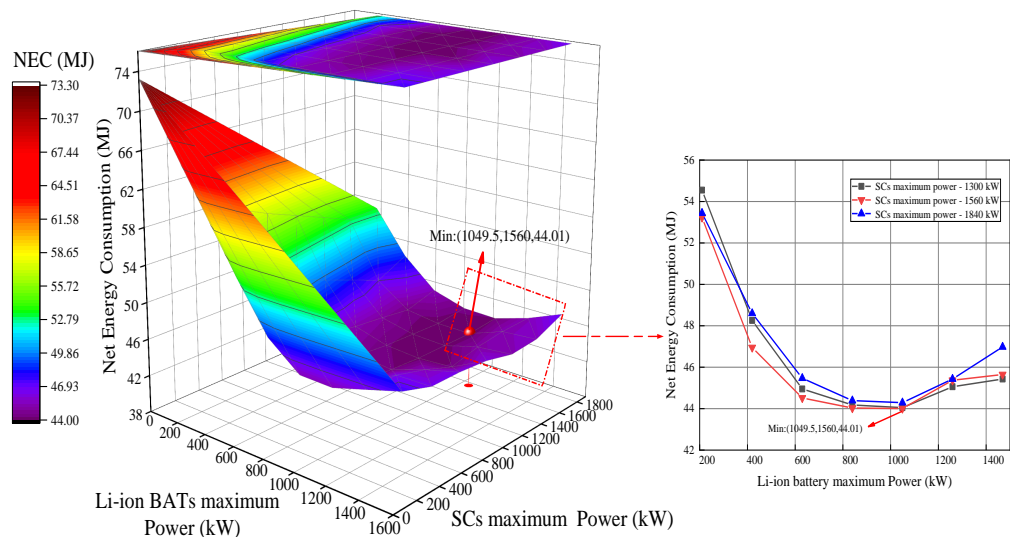
Figure 8. The NEC for different maximum power of on-board HESDs under varying capital cost constraints.

Figure 9 illustrates the detailed trend shownig how the total power and mass of on-board HESDs influence the NEC solutions. It clearly indicates that even though the maximum power of on-board HESDs continually increases, the NEC cannot be continuously

reduced, and even raises slightly due to the increase in the total mass of on-board HESDs, and the NEC solutions slightly increased from 44.01 MJ to 46.98 MJ. This further reveals that, with the given railway line and journey time, the optimal on-board HESDs' power split scheme can achieve the unique minimum NEC solution, which allows for railway planners and operators to avoid an unnecessary waste of on-board HESDs capacity and reduce operation costs.
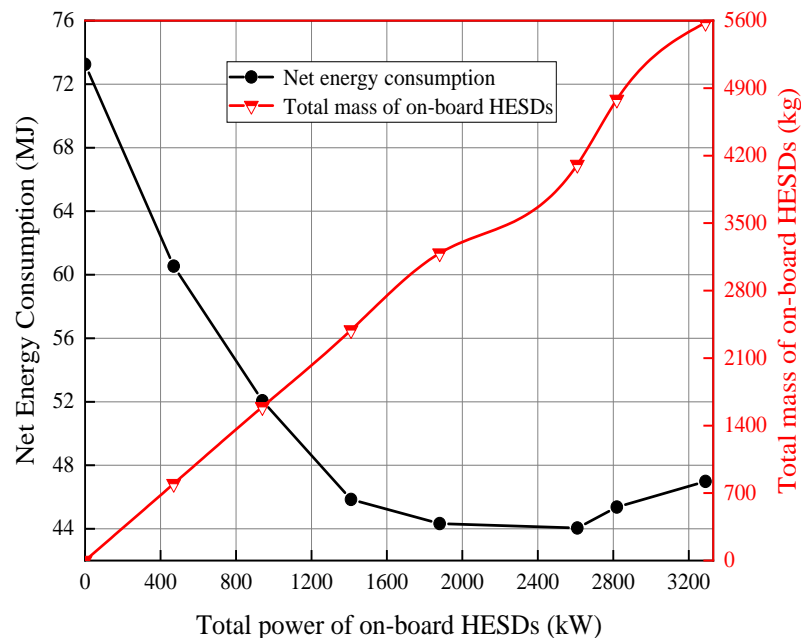

Figure 9. Relationship between NEC and total mass of on-board HESDs with different sizes.

4.2. Impact of Different Initial SOC of On-Board HESDs on Train Operation

This subsection aims to further explore the impact of the different initial SOC for on-board HESDs, which is another important engineering characteristic of on-board HESDs and impacts train optimal operation. In cases 4–6, the maximum power of the Li-ion BATs and the SCs were uniformly set at 1049.6 kW and 1560 kW, respectively. The initial SOC for the on-board HESDs was set to 30%, 60%, and 90% in cases 4–6, respectively. The parameters and optimal results for cases 4–6 are tabulated in Tables 6.

Table 6. The parameters and optimization results for cases 4–6.

Case	4	5	6
Li-ion BATs maximum power (kW)	1049.6	1049.6	1049.6
Li-ion BATs electric energy (kWh)	258.75	258.75	258.75
Capital cost (¥)	450,000	450,000	450,000
Initial SOC for Li-ion BATs (%)	30	60	90
SCs maximum power (kW)	1560	1560	1560
SCs electric energy (kWh)	1.68	1.68	1.68
Capital cost (¥)	540,000	540,000	540,000
Initial SOC for SCs (%)	30	60	90
NEC (MJ)	45.09	43.89	45.41

When the initial SOC of on-board HESDs is different, it indicates that on-board HESDs power split schemes for different cases need to meet the constraints of the proposed model and achieve the energy-saving operation for electric trains. In Figures 10 and 11, the speed trajectory for case 4 does not demonstrate a notable change compared with case 5, while the power profiles of on-board HESDs and the feeding TSSs have significant differences. As shown in Figure 11a, when the journey time ranges from 0 s to 24 s, the propulsion energy

of the train only comes from the feeding TSSs, and on-board HESDs cannot be allowed to discharge to support traction operations due to their minimum allowable SOC value. Therefore, a higher NEC value is observed in case 4 and the maximal peak power is found from the feeding TSSs consumed by the train. However, it can be observed that on-board HESDs with a higher initial SOC are not always preferred in terms of NEC values. From Figure 11c, it is easily noted when the train operates from 6 s to 14 s and 104 s to 112 s, the traction energy of the train mainly derives from the on-board HESDs.
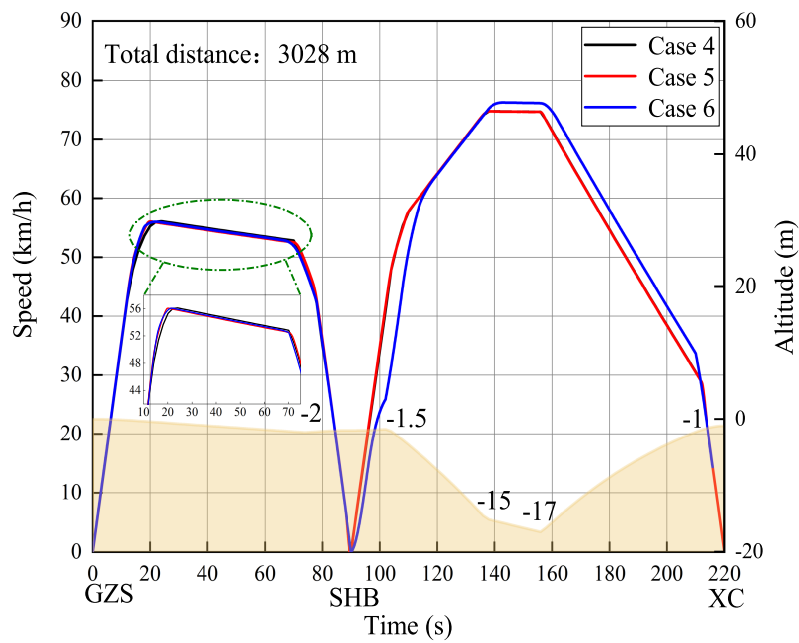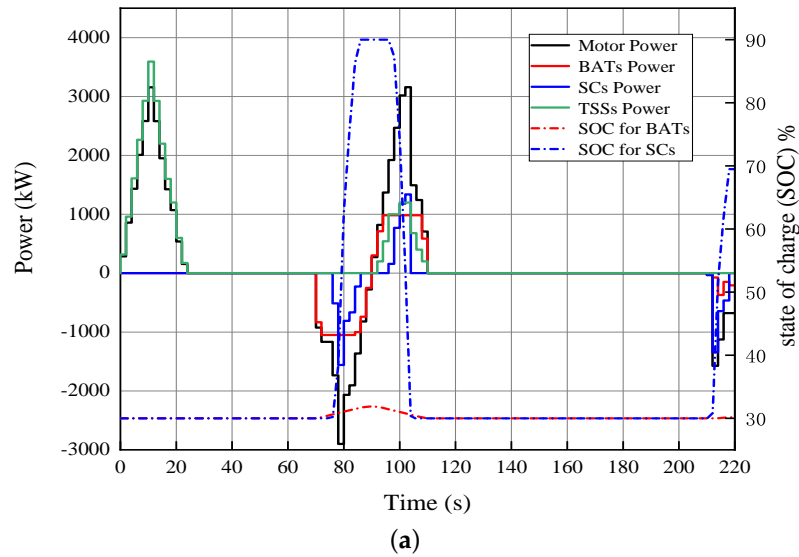
Figure 10. The optimal speed trajectories and altitude profile for cases 4–6.

(**a**)

Figure 11. *Cont.*

(b)

(c)
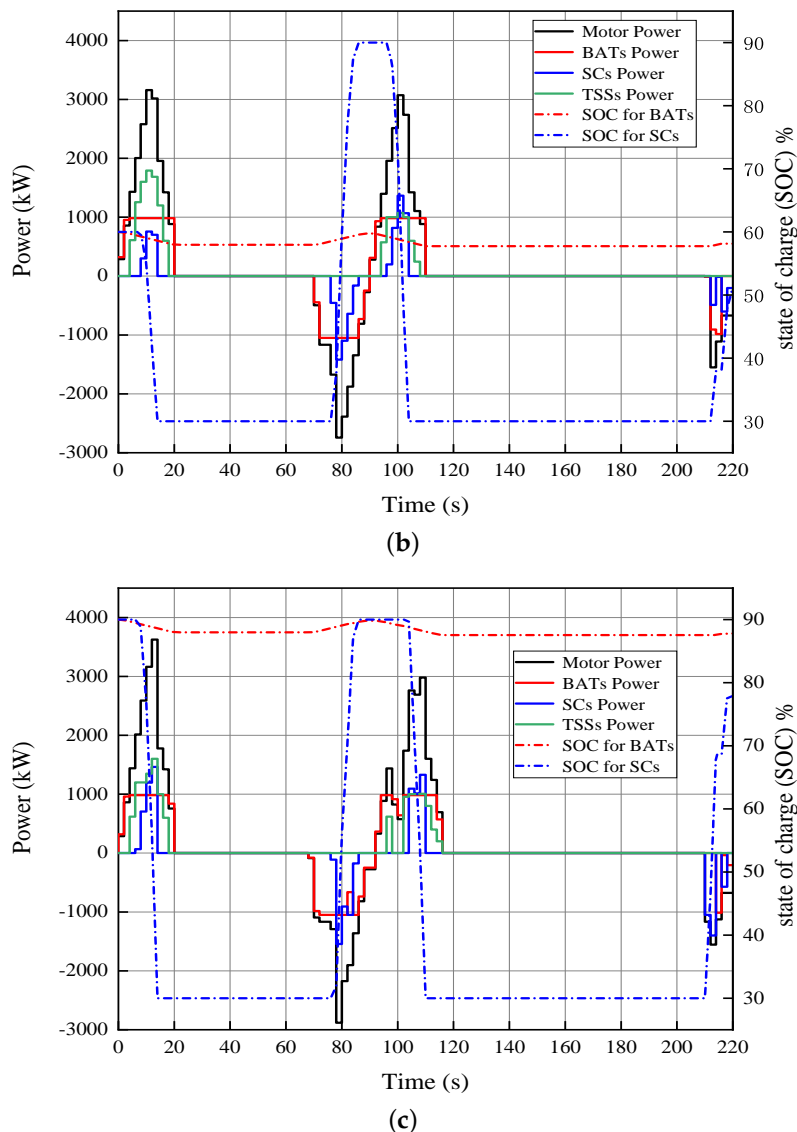
Figure 11. The motor power, TSSs power, discharge/charge power of on-board HESDs and SOC curves for cases 4–6. (**a**) case 4. (**b**) case 5. (**c**) case 6.

This results from on-board HESDs with excessive initial SOC because, for energy-saving operations, they need to be discharged first to obtain sufficient rechargeable capacity for subsequent braking operations. As shown in Figure 12, although the traction energy consumption from the feeding TSSs in case 4 was significantly higher than that in case 6, the frequent discharging process undermines the energy-saving potential.

Based on the above optimization results, Figure 13 further depicts the relationship between the different initial SOC of on-board HESDs and the NEC, which helps railway vehicle operators to dynamically adjust the charging/discharging strategy of on-board HESDs and take full advantage of on-board HESDs for energy-efficient operation. In Figure 13, the initial SOC range of on-board HESDs is from 30% to 90% with an increment step of 10%, and when the initial SOC of Li-ion BATs and SCs is set as 50% and 70%, the proposed model obtains the minimum NEC, i.e., 43.61 MJ. In addition, a lower or excessive initial SOC cannot obtain the optimal NEC solution for the given railway line and journey time conditions. It can be concluded that the optimization results for different initial SOCs show substantial differences, and we need to obtain a trade-off between the initial SOC of Li-ion BATs and SCs to improve the energy-saving potential of on-board HESDs.
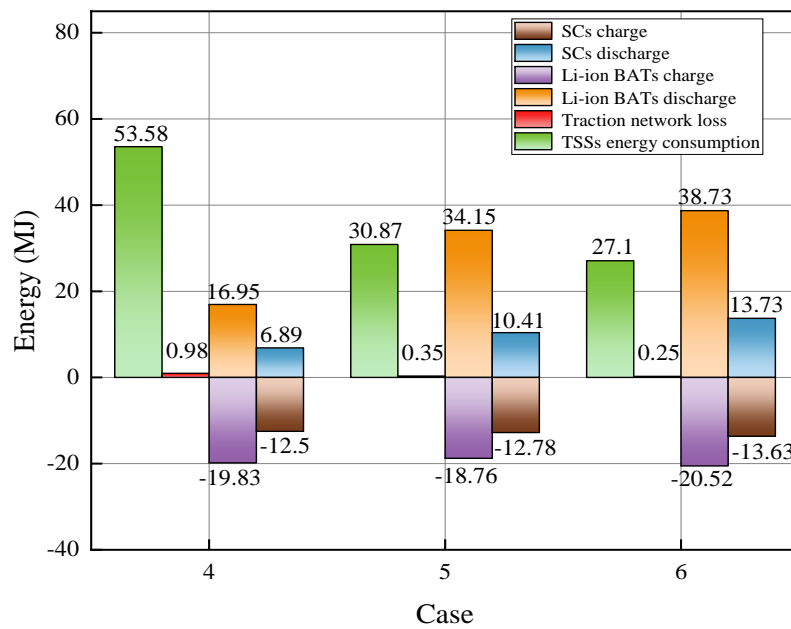
**Figure 12.** The energy flow of all the components in cases 4–6.
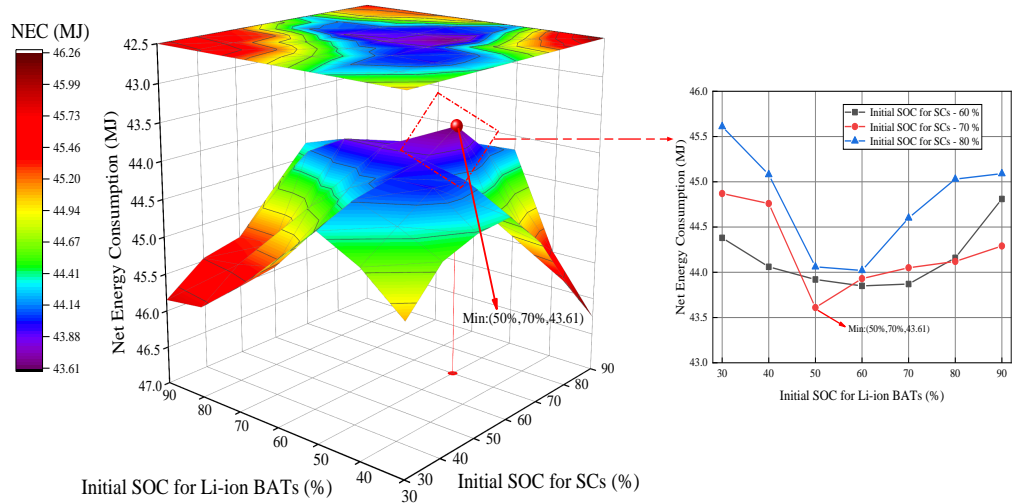
Figure 13. The NEC for different initial SOC of on-board HESDs.

4.3. Impact of the Degradation of Li-Ion BATs on Train Operation

The cases above all operate under the assumption that the optimization problem is solved over a horizon (train travel distance) that is a negligible fraction of the total distance to reach the on-board HESDs' end of life. In other words, the influence of the on-board HESDs' degradation process on the train operation can be neglected. However, in real operation, on-board HESDs would suffer from degradation considering the long-term train operation. Concerning SCs, they can achieve a longer cycle lifetime, e.g., from 80,000 to 100,000 cycles, as previously mentioned [10]. Therefore, from the perspective of long-term energy-saving operation, it also seems logical to focus only on exploring the impact of the degradation behavior of Li-ion BATs with a limited lifespan on train operation.

Figure 14 shows the schematic representation of the electrochemical Li-ion battery function, which consists of three regions: an anode (negative electrode), a separator, and a cathode (positive electrode). During the discharging operation, the electrons and ions simultaneously flow from the anode to the cathode through an external circuit and electrolyte, respectively. The process is reversed, and the ion flow is from the cathode to the anode during the charging operation. The performance of Li-ion BATs irreversibly generates

deterioration after long-term charging and discharging operations. The determining factors for Li-ion battery degradation are usually defined as capacity fading and internal resistance rising [46].

(1) Capacity fading: During the Li-ion BATs operatiom, the chemical reaction between the anode and the electrolyte and the simultaneous consumption of lithium ions would lead to capacity fading. Keeping the Li-ion BATs at a high cycling rate would enhance the degradation degree [47]. The capacity fading of Li-ion BATs would shorten the electric trains' achievable range and it is considered to reach the end-of-life when the available capacity is 80% of the nominal capacity [48].

(2) Internal resistance rising: After long-term cycling of Li-ion BATs, the decrease in accessible surface area due to continuous solid electrolyte interphase (SEI) growth can also cause internal resistance to rise. Charge/discharge operation or high temperatures tend to accelerate the degradation process [47]. The internal resistance raises, thereby reducing the available output power of the Li-ion BATs, and increased to 160% of its original value under the reference operating conditions, which is typically considered to be the end-of-life [49,50].
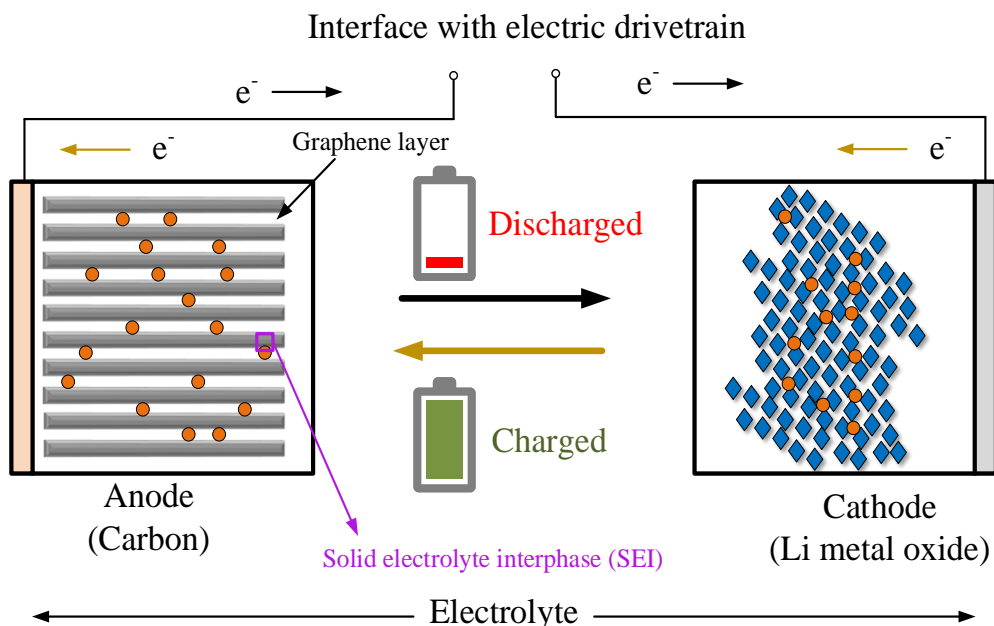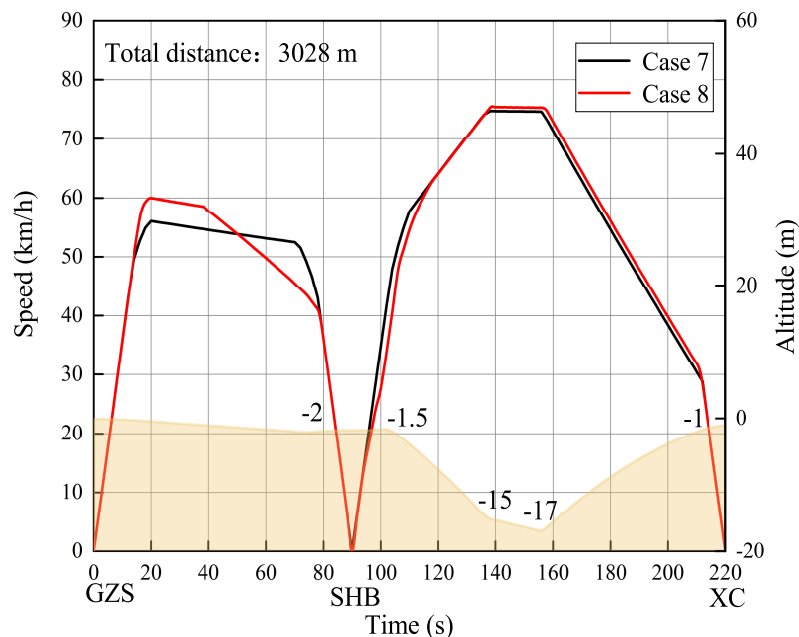

Figure 14. The schematic representation of electrochemical Li-ion battery cell model.

For the analysis stated above, the presence and extent of different Li-ion BATs degradation mechanisms and their multiple interaction relationships make it very complicated to accurately model and estimate the impact of degradation behaviors on optimal train operation. The purpose of this subsection is to synthesize the key degradation parameters of Li-ion BATs (i.e., their capacity and internal resistance) for a sensitivity analysis from an operations research perspective, as well as to reveal the effect of degradation behavior on NEC values in the context of transportation planning problems. The analytical method combines the advantages of the electrochemical modeling approach and traditional empirical approach, and is thus simpler than the former while being applicable to broader conditions than the latter. Here, we used the optimization results in Figure 13 as an example to further explore the influence of Li-ion battery degradation behavior on train operation. The parameters and optimal results for cases 7–8 are tabulated in Table 7.

Table 7. The parameters and optimization results for cases 7–8.

Case	7	8
Li-ion BATs maximum power (kW)	1049.6	1049.6
Li-ion BATs capacity fading ratio (%)	0	20
Li-ion BATs internal resistance rising ratio (%)	0	60
Initial SOC (%)	50	50
SCs maximum power (kW)	1560	1560
Initial SOC (%)	70	70
NEC (MJ)	43.61	50.82

In case 7, the degradation of the Li-ion BATs was not considered for comparison, and they were treated as fresh cells. Therefore, the capacity fading ratio and the internal resistance rising ratio are 0. From Figures 15 and 16, it can be observed that the railway vehicle tends to utilize longer braking distances as well as the charging process for energy-saving operation in case 8 when the journey time ranges from 38 s to 90 s.

Figure 15. The optimal speed trajectories and altitude profile for cases 7–8.

Furthermore, the maximum charge/discharge power of the Li-ion BATs in case 8 is significantly less than that in case 7, which indicates that, as the internal resistance increases, the Li-ion BATs should be employed as little as possible to avoid unnecessary internal energy loss. Therefore, it can be concluded that the train needs to dynamically adjust the initial optimal speed trajectory with the increase in the degradation degree of the on-board Li-ion BATs. In other words, the energy-saving potential of degraded Li-ion BATs is more dependent on the power split strategy, especially when the internal resistance increases and the electric trains tend to consume more energy from the feeding TSSs rather than Li-ion BATs. Compared to fresh cells, the degraded Li-ion BATs could no longer implement the initial power split strategy, which leads to greater internal losses.
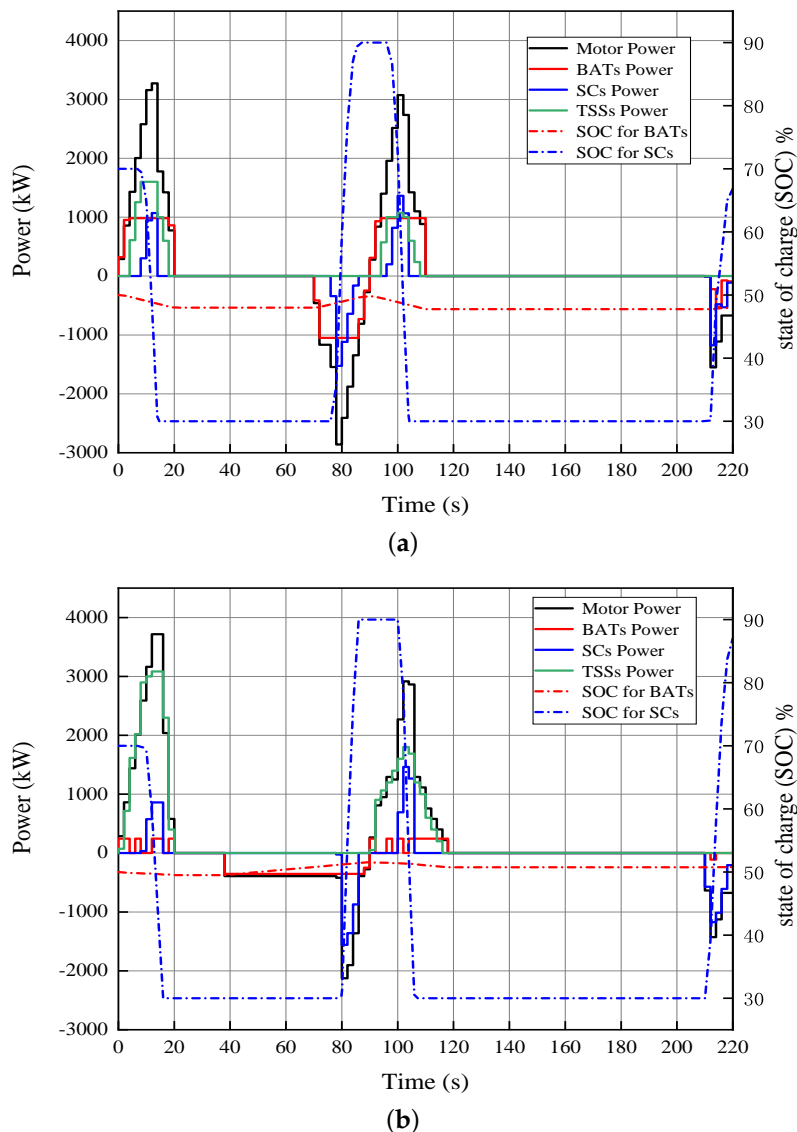
Figure 16. The motor power, TSSs power, discharge/charge power of on-board HESDs and SOC curves for cases 7–8. (**a**) case 7. (**b**) case 8.

Based on the above optimization results, Figure 17 further depicts the relationship between the NEC solutions and capacity fading ratio and resistance rising ratio, whose performances are the key factors concerning the railway energy systems planners and operators after considering the degradation of Li-ion BATs due to the long-term train operation. From Figure 17, it should be noted that the NEC solutions increase more slowly when the capacity fading ratio of the Li-ion BATs rises. The NEC solutions for the internal resistance rising ratio of Li-ion BATs are more sensitive, and lead to higher NEC solutions in some spaces. The results clearly show that the increase in internal resistance caused by high temperature or over-charge/discharge operations is more worthy of our attention than the capacity degradation, which would greatly reduce the available output power of Li-ion BATs and is the main factor undermining the energy-saving operation for electric trains.
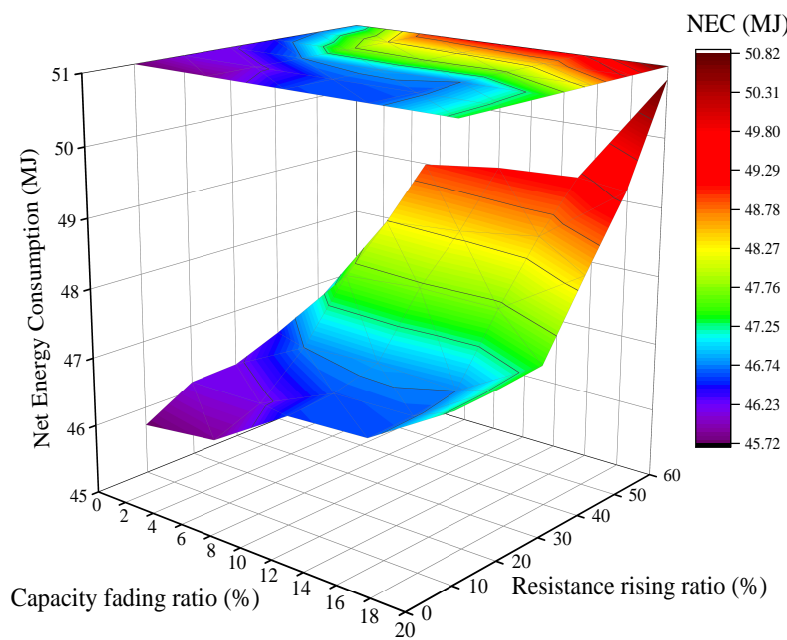
Figure 17. The NEC under varying capacity fading ratio and internal resistance rising ratio of Li-ion BATs.

4.4. The Analysis of Energy-Saving Potential

The net energy consumption and energy-saving rate for cases 2–8 are plotted in Figure 18. Note that the energy-saving rate of the abovementioned cases is calculated in reference to case 1 without on-board HESDs. Figure 18 shows that by optimizing the capacity and initial SOC of on-board HESDs, it is indeed possible to achieve energy-saving operation for electric trains in the given journey.
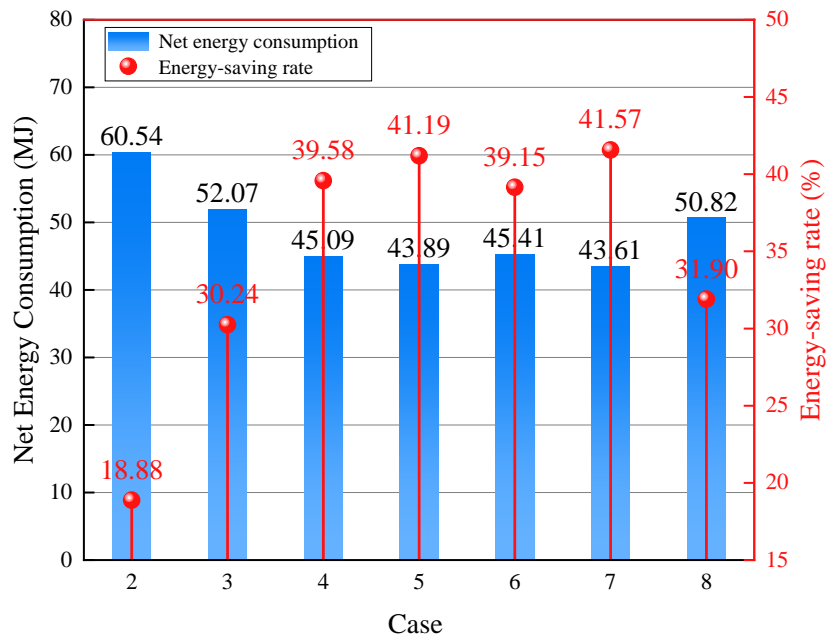

Figure 18. The net energy consumption and energy-saving rate for cases 2–8.

When the initial SOC of the on-board HESDs remains unchanged in cases 2 and 3, the NEC decreases and the energy-saving rate rises by increasing the maximum power and capacity of the on-board HESDs. However, Figure 8 clearly shows that by continuously increasing the power and capacity of the on-board HESDs, the NEC solutions slightly

increase due to the increase in total mass. As a result, the minimum NEC can only be obtained when the power and capacity of the on-board HESDs change and the initial SOC remains unchanged. In addition, the lower or excessive initial SOC of the on-board HESDs could undermine the energy-saving potential of integrated systems in cases 4–6 when the optimal capacity is obtained. It is worth mentioning that although the energy-saving rate of railway vehicles could reach up to 41.57% in case 7, after considering the long-term train operation, the energy-saving rate would drop to 31.90% in case 8 due to the degradation of Li-ion BATs. The optimization results provide clear guidance on how to select and utilize on-board HESDs and avoid unnecessary waste in real engineering applications.

5. Conclusions

In this paper, a time-based MILP model was developed, which aims to optimize the energy-saving operation of electric trains equipped with on-board HESDs in DC railway systems. The main attractiveness of the proposed integration power flow model resides in the combination of the optimal energy-saving operation with the emerging on-board HESDs under different constraints. The minimum NEC solution can be obtained to reveal the energy-saving potential of on-board HESDs in practical engineering applications, which are the key factors in railway energy system planners and operators. In addtion, the real-world train operation data from Guangzhou Metro Line No.7 and mature commercial components are applied in the proposed model.

Based on the abovementioned case studies, it can be concluded that different capacity of on-board HESDs would change the energy-saving operation for electric trains and charging/discharging strategy, which leads to notable differences in the train speed trajectory and power split. More specifically, the NEC value is reduced to 44.01 MJ when the maximum power of the Li-ion BATs and the SCs is 1049.6 kW and 1560 kW, respectively. However, the NEC value would not be continuously reduced, and could even rise slightly due to the increase in the total mass of on-board HESDs, which increased slightly from 44.01 MJ to 46.98 MJ. Furthermore, the lower or excessive initial SOC for on-board HESDs would undermine the energy-saving potential of the integrated system. It can be observed that the proposed model obtains the minimum NEC, i.e., 43.61 MJ, under different initial SOC constraints for on-board HESDs. Overall, the research results show that the optimal energy-saving operation equipped with on-board HESDs requires trade-offs under different capacities and initial SOC constraints. Considering the degradation of Li-ion BATs due to the long-term train operation, the increase in internal resistance leads to a lower available output power and higher NEC compared with capacity fading. The degradation changed the energy-saving operation for electric trains and the NEC value, where the energy-saving rate decreased from 41.57% to 31.90%. In short, based on the proposed integration power flow model, the optimization results show significant correlations between on-board HESDs and energy-saving operation for electric trains, which further demonstrate the necessity of research.

In future work, it is our intention to extend the existing research, considering more complex traffic and energy system setups, such as by involving wayside energy storage devices, multiple electric trains and or distributed energy sources such as photovoltaics and wind power.

Author Contributions: B.Z. wrote the original draft and designed the experiments; S.L. provided funding acquisition, methodology, and supervision. Y.P. analyzed the data and code; C.W. contributed to the methodology and investigation; G.M. and M.F. provided software development and specifically visualization. B.L. reviewed and revised the paper. All authors have read and agreed to the published version of the manuscript.

Abbreviations

The following abbreviations are used in this manuscript:

HESDs	Hybrid Energy Storage Devices
MILP	Mixed Integer Linear Programming
SOC	State of Charge
NEC	Net Energy Consumption
BATs	Batteries
SCs	Supercapacitors
TSSs	Traction Substations
SOH	State of Health
PWL	Piecewise Linearization
DC	Direct Current
SEI	Solid Electrolyte Interphase

Appendix A

Appendix A.1. Piecewise Linear Method

In the proposed time-based MILP model, the PWL method was adopted to deal with a series of nonlinear variables related to speed. The special ordered set type 2 (SOS2) was applied in the PWL method to efficiently simplify nonlinear variable relationships, which can increase the calculation speed and reduce the complexity of the proposed model. SOS2 contains a series of nonnegative variables to represent a nonlinear function, where only two adjacent variables are greater than 0 and the sum of all variables is equal to 1. The variables of SOS2 satisfy the constraints as follows:

$$\sum_{c=1}^{C} \alpha_{i,j}^{c} = 1. \tag{A1}$$

$$0 \leq \alpha_{i,j}^{c} \leq 1, \quad c = 1, 2, 3 \ldots C \tag{A2}$$

where $\alpha_{i,j}^{c}$ are variables of SOS2 and the constant C is the total number of variables for each $\Delta t_{i,j}$. To linearize the nonlinear constraints in (2), (3), (4), and (18), $\delta_{i,j}$ is set to a small constant and denotes the linear part from the minimum speed $V_{i,j,\min}$ to the maximum speed $V_{i,j,\max}$, which could be obtained by:

$$\delta_{i,j} = \frac{\left(V_{i,j,\max} - V_{i,j,\min}\right)}{C}. \tag{A3}$$

When $\delta_{i,j}$ increase, the accuracy of the model will be improved, but the calculation time of the model will also be significantly longer. As a result, the decision variables $V_{i,j}$ and $V_{i,j}^{2}$ can be approximated as $V_{i,j}'$ and $V_{i,j}'^{2}$, respectively. The relevant constraints are shown as follows:

$$
\begin{cases}
V_{i,j} \approx V'_{i,j} = \displaystyle\sum_{c=1}^{C} \left(V_{i,j,\min} + (c-1)\delta_{i,j}\right) \cdot \alpha^c_{i,j} \\[4mm]
V^2_{i,j} \approx V'^2_{i,j} = \displaystyle\sum_{c=1}^{C} \left(V_{i,j,\min} + (c-1)\delta_{i,j}\right)^2 \cdot \alpha^c_{i,j}.
\end{cases}
\tag{A4}
$$

Similarly, the approximation of the decision variables related to average speed $V_{i,j,ave}$ and $V^2_{i,j,ave}$ in (5) can be expressed by:

$$
\begin{cases}
V_{i,j,\,\text{ave}} \approx V'_{i,j,\,\text{ave}} = \displaystyle\sum_{c=1}^{C} \left(V_{i,j,\min} + (c-1)\delta_{i,j}\right) \cdot \beta^c_{i,j} \\[4mm]
V^2_{i,j,\,\text{ave}} \approx V'^2_{i,j,\,\text{ave}} = \displaystyle\sum_{c=1}^{C} \left(V_{i,j,\min} + (c-1)\delta_{i,j}\right)^2 \cdot \beta^c_{i,j}
\end{cases}
\tag{A5}
$$

where $\beta^c_{i,j}$ are variables of SOS2. Likewise, for the sake of compactness, the variable $I_{bat}(t)$ in (7) and the variable $I_{sc}(t)$ in (10) are linearized by the abovementioned method. From (14), it can be observed that the nonlinear constraint cannot be directly solved. Therefore, this can be further derived as:

$$
\begin{cases}
P_{sub}(t) = U_{sub}[I_{Tss1}(t) + I_{Tss2}(t)] \\[2mm]
P_{tr}(t) = U_{tr}(t)[I_{Tss1}(t) + I_{Tss2}(t)]
\end{cases}
\tag{A6}
$$

where $I_{Tss1}(t)$ and $I_{Tss2}(t)$ are the currents flowing through the feeding TSS 1 and feeding TSS 2, respectively. By introducing four new variables $Z_1(t)$, $Z_2(t)$, $Z_3(t)$, and $Z_4(t)$, the nonlinear constraint can be converted into a separable form as follows:

$$
\begin{cases}
Z_1(t) = \dfrac{1}{2}[U_{tr}(t) + I_{Tss1}(t)] \\[3mm]
Z_2(t) = \dfrac{1}{2}[U_{tr}(t) - I_{Tss1}(t)] \\[3mm]
Z_3(t) = \dfrac{1}{2}[U_{tr}(t) + I_{Tss2}(t)] \\[3mm]
Z_4(t) = \dfrac{1}{2}[U_{tr}(t) - I_{Tss2}(t)].
\end{cases}
\tag{A7}
$$

Then, we can derive the nonlinear variable $P_{tr}(t)$ as follows:

$$
\begin{aligned}
P_{tr}(t) &= U_{tr}(t)I_{Tss1}(t) + U_{tr}(t)I_{Tss2}(t) \\
&= \left(Z_1^2(t) - Z_2^2(t)\right) + \left(Z_3^2(t) - Z_4^2(t)\right).
\end{aligned}
\tag{A8}
$$

Similarly, the piecewise linear of new variables $Z_1^2(t)$, $Z_2^2(t)$, $Z_3^2(t)$, and $Z_4^2(t)$ can be obtained by applying the above-mentioned SOS2 variable sets. $\gamma^k_{i,j}$ are another variables of SOS2, and $\Theta_{i,j}$ is set to a small constant, which denotes the linear part from the minimum value $Z^2_{J,min}(J = 1, 2, 3, 4)$ to the maximum value $Z^2_{J,max}$. They can be formulated by:

$$
\sum_{k=1}^{K} \gamma^k_{i,j} = 1.
\tag{A9}
$$

$$
0 \leq \gamma^k_{i,j} \leq 1, \quad k = 1, 2, 3 \dots K.
\tag{A10}
$$

$$
\begin{cases}
\Theta_{1,i,j} = \dfrac{\left(Z_{1,max}^2 - Z_{1,min}^2\right)}{K} \\[2ex]
\Theta_{2,i,j} = \dfrac{\left(Z_{2,max}^2 - Z_{2,min}^2\right)}{K} \\[2ex]
\Theta_{3,i,j} = \dfrac{\left(Z_{3,max}^2 - Z_{3,min}^2\right)}{K} \\[2ex]
\Theta_{4,i,j} = \dfrac{\left(Z_{4,max}^2 - Z_{4,min}^2\right)}{K}.
\end{cases}
\tag{A11}
$$

The approximation of new variables $Z_1^2(t)$, $Z_2^2(t)$, $Z_3^2(t)$, and $Z_4^2(t)$ can be calculated by:

$$
\begin{cases}
Z_1^2(t) \approx Z_1'^2(t) = \displaystyle\sum_{k=1}^{K}\left(Z_{1,min}^2 + (k-1)\Theta_{1,i,j}\right)\cdot\gamma_{i,j}^k \\[2ex]
Z_2^2(t) \approx Z_2'^2(t) = \displaystyle\sum_{k=1}^{K}\left(Z_{2,min}^2 + (k-1)\Theta_{2,i,j}\right)\cdot\gamma_{i,j}^k \\[2ex]
Z_3^2(t) \approx Z_3'^2(t) = \displaystyle\sum_{k=1}^{K}\left(Z_{3,min}^2 + (k-1)\Theta_{3,i,j}\right)\cdot\gamma_{i,j}^k \\[2ex]
Z_4^2(t) \approx Z_4'^2(t) = \displaystyle\sum_{k=1}^{K}\left(Z_{4,min}^2 + (k-1)\Theta_{4,i,j}\right)\cdot\gamma_{i,j}^k.
\end{cases}
\tag{A12}
$$

References

1.　Sun, H.; Wu, J.; Ma, H.; Yang, X.; Gao, Z. A Bi-Objective Timetable Optimization Model for Urban Rail Transit Based on the Time-Dependent Passenger Volume. *IEEE Trans. Intell. Transp. Syst.* **2019**, *20*, 604–615. [CrossRef]
2.　Hu, H.; Zheng, Z.; He, Z.; Wei, B.; Wang, K.; Yang, X.; Wei, W. The framework and key technologies of traffic energy internet. *Proc. CSEE* **2018**, *38*, 12–24.
3.　Ceraolo, M.; Lutzemberger, G. Stationary and on-board storage systems to enhance energy and cost efficiency of tramways. *J. Power Sources* **2014**, *264*, 128–139. [CrossRef]
4.　Ghaviha, N.; Campillo, J.; Bohlin, M.; Dahlquist, E. Review of Application of Energy Storage Devices in Railway Transportation. *Energy Procedia* **2017**, *105*, 4561–4568. [CrossRef]
5.　Araújo, R.E.; de Castro, R.; Pinto, C.; Melo, P.; Freitas, D. Combined Sizing and Energy Management in EVs with Batteries and Supercapacitors. *IEEE Trans. Veh. Technol.* **2014**, *63*, 3062–3076. [CrossRef]
6.　Peng, F.; Zhao, Y.; Li, X.; Liu, Z.; Chen, W.; Liu, Y.; Zhou, D. Development of master-slave energy management strategy based on fuzzy logic hysteresis state machine and differential power processing compensation for a PEMFC-LIB-SC hybrid tramway. *Appl. Energy* **2017**, *206*, 346–363. [CrossRef]
7.　Ogasa, M. Application of Energy Storage Technologies for Electric Railway Vehicles—Examples with Hybrid Electric Railway Vehicles. *IEEJ Trans. Electr. Electron. Eng.* **2010**, *5*, 1001–1012. [CrossRef]
8.　Hayashiya, H.; Suzuki, T.; Kawahara, K.; Yamanoi, T. Comparative study of investment and efficiency to reduce energy consumption in traction power supply: A present situation of regenerative energy utilization by energy storage system. In Proceedings of the 2014 16th International Power Electronics and Motion Control Conference and Exposition, Antalya, Turkey, 21–24 September 2014; Volume 1, pp. 685–690.
9.　Rufer, A.C. Energy storage for railway systems, energy recovery and vehicle autonomy in Europe. In Proceedings of the 2010 International Power Electronics Conference-ECCE ASIA-, Sapporo, Japan, 21–24 June 2010; Volume 1, pp. 3124–3127.
10.　Koohi-Fayegh, S.; Rosen, M.A. A review of energy storage types, applications and recent developments. *J. Energy Storage* **2020**, *27*, 101–114. [CrossRef]
11.　Kumar, Y.A.; Kumar, K.D.; Kim, H.J. A novel electrode for supercapacitors: Efficient PVP-assisted synthesis of Ni_3S_2 nanostructures grown on Ni foam for energy storage. *Dalton Trans.* **2020**, *49*, 4050–4059. [CrossRef]
12.　Kumar, Y.A.; Kim, H.J. Preparation and electrochemical performance of $NiCo_2O_4$@$NiCo_2O_4$ composite nanoplates for high performance supercapacitor applications. *New J. Chem.* **2018**, *42*, 19971–19978. [CrossRef]
13.　Yedluri, A.K.; Kulurumotlakatla, D.K.; Sangaraju, S.; Obaidat, I.M.; Kim, H.-J. Facile synthesis of novel and highly efficient $CoNi_2S_4$-$Ni(OH)_2$ nanosheet arrays as pseudocapacitive-type electrode material for high-performance electrochemical supercapacitors. *J. Energy Storage* **2020**, *31*, 101623–101631. [CrossRef]
14.　Brenna, M.; Bucci, V.; Falvo, M.C.; Foiadelli, F.; Ruvio, A.; Sulligoi, G.; Vicenzutti, A. A Review on Energy Efficiency in Three Transportation Sectors: Railways, Electrical Vehicles and Marine. *Energies* **2020**, *2*, 2378. [CrossRef]

15. Dragoni, E. Mechanical design of flywheels for energy storage: A review with state-of-the-art developments. *Proc. Inst. Mech. Eng. Part L J. Mater. Des. Appl.* **2019**, *233*, 995–1004. [CrossRef]

16. Spiryagin, M.; Wolfs, P.J.; Szanto, F.; Sun, Y.Q.; Cole, C.; Nielsen, D. Application of flywheel energy storage for heavy haul locomotives. *Appl. Energy* **2015**, *157*, 607–618. [CrossRef]

17. Zhao, N.; Tian, Z.; Chen, L.; Roberts, C.; Hillmansen, S. Driving Strategy Optimization and Field Test on an Urban Rail Transit System. *IEEE Intell. Transp. Syst. Mag.* **2021**, *13*, 34–44. [CrossRef]

18. Nallaperuma, S.; Fletcher, D.; Harrison, R. Optimal control and energy storage for DC electric train systems using evolutionary algorithms. *Railw. Eng. Sci.* **2021**, *3*, 104–114. [CrossRef]

19. Zhang, B.; Wu, C.; Meng, G.; Xue, F.; Lu, S. Optimal Sizing of Onboard Hybrid Energy Storage Devices Considering the Long-Term Train Operation. *IEEE Access* **2022**, *10*, 58360–58374. [CrossRef]

20. Meng, G.; Wu, C.; Zhang, B.; Xue, F.; Lu, S. Net Hydrogen Consumption Minimization of Fuel Cell Hybrid Trains Using a Time-Based Co-Optimization Model. *Energies* **2022**, *5*, 2891. [CrossRef]

21. Wu, C.; Lu, S.; Xue, F.; Jiang, L.; Yang, J. Optimization of Speed Profile and Energy Interaction at Stations for a Train Vehicle with On-board Energy Storage Device. In Proceedings of the 2018 IEEE Intelligent Vehicles Symposium (IV), Changshu, China, 26–30 June 2018; Volume 1, pp. 773–780.

22. Zhang, W.; Li, J.; Xu, L.; Ouyang, M. Optimization for a fuel cell/battery/capacity tram with equivalent consumption minimization strategy. *Energy Convers. Manag.* **2017**, *134*, 59–69. [CrossRef]

23. Noda, Y.; Miyatake, M. Methodology to apply dynamic programming to the energy-efficient driving technique of lithium-ion battery trains. In Proceedings of the 2016 International Conference on Electrical Systems for Aircraft, Railway, Ship Propulsion and Road Vehicles & International Transportation Electrification Conference (ESARS-ITEC), Toulouse, France, 2–4 November 2016; Volume 1, pp. 1–6.

24. Sumpavakup, C.; Ratniyomchai, T.; Kulworawanichpong, T. Optimal energy saving in DC railway system with on-board energy storage system by using peak demand cutting strategy. *J. Mod. Transp.* **2017**, *25*, 223–235. [CrossRef]

25. Xia, H.; Yang, Z.; Lin, F.; Chen, H. Modeling and state of charge-based energy management strategy of ultracapacitor energy storage system of urban rail transit. In Proceedings of the IECON 2015—41st Annual Conference of the IEEE Industrial Electronics Society, Yokohama, Japan, 9–12 November 2015; Volume 3, pp. 2082–2087.

26. Yang, H.; Shen, W.; Yu, Q.; Liu, J. Coordinated demand response of rail transit load and energy storage system in considering driving comfort. *CSEE J. Power Energy Syst.* **2020**, *2*, 1131–1145.

27. Pelletier, S.; Jabali, O.; Laporte, G.; Veneroni, M. Battery degradation and behaviour for electric vehicles: Review and numerical analyses of several models. *Transp. Res. Part B-Methodol.* **2017**, *103*, 158–187. [CrossRef]

28. Kuntz, P.; Raccurt, O.; Azaïs, P.; Richter, K.; Waldmann, T.; Wohlfahrt-Mehrens, M.; Bardet, M.; Buzlukov, A.; Génies, S. Identification of Degradation Mechanisms by Post-Mortem Analysis for High Power and High Energy Commercial Li-Ion Cells after Electric Vehicle Aging. *Batteries* **2021**, *7*, 48. [CrossRef]

29. Arrinda, M.; Oyarbide, M.; Macicior, H.; Muxika, E. Unified Evaluation Framework for Stochastic Algorithms Applied to Remaining Useful Life Prognosis Problems. *Batteries* **2021**, *7*, 35. [CrossRef]

30. Zhang, J.; Li, X.; Zhang, G.; Guo, J.; Huang, Q.; Wang, C.; Zhou, D.; Wei, D. Experimental investigation on the essential cause of the degrading performances for an overcharging ternary battery. *Int. J. Energy Res.* **2020**, *44*, 3134–3147. [CrossRef]

31. Li, S.; He, H.; Su, C.; Zhao, P. Data driven battery modeling and management method with aging phenomenon considered. *Appl. Energy* **2020**, *275*, 115340–115352. [CrossRef]

32. Lee, P.; Park, S.; Cho, I.; Kim, J. Vibration-based degradation effect in rechargeable lithium ion batteries having different cathode materials for railway vehicle application. *Eng. Fail. Anal.* **2021**, *124*, 105334–105347. [CrossRef]

33. Huang, M. Incremental Capacity Analysis-Based Impact Study of Diverse Usage Patterns on Lithium-Ion Battery Aging in Electrified Vehicles. *Batteries* **2019**, *5*, 59. [CrossRef]

34. Lin, H.; Kang, L.; Xie, D.; Linghu, J.; Li, J. Online State-of-Health Estimation of Lithium-Ion Battery Based on Incremental Capacity Curve and BP Neural Network. *Batteries* **2022**, *8*, 29. [CrossRef]

35. Wu, C.; Xu, B.; Lu, S.; Xue, F.; Jiang, L.; Chen, M. Adaptive Eco-Driving Strategy and Feasibility Analysis for Electric Trains With Onboard Energy Storage Devices. *IEEE Trans. Transp. Electrif.* **2021**, *7*, 1834–1848. [CrossRef]

36. Xiao, Z.; Feng, X.; Wang, Q.; Sun, P. Eco-driving control for hybrid electric trams on a signalised route. *IET Intell. Transp. Syst.* **2019**, *14*, 36–44. [CrossRef]

37. Wu, C.; Lu, S.; Xue, F.; Jiang, L.; Chen, M. Optimal Sizing of Onboard Energy Storage Devices for Electrified Railway Systems. *IEEE Trans. Transp. Electrif.* **2020**, *6*, 1301–1311. [CrossRef]

38. Kim, Y.; Figueroa-Santos, M.A.; Prakash, N.; Baek, S.S.; Siegel, J.B.; Rizzo, D.M. Co-optimization of speed trajectory and power management for a fuel-cell/battery electric vehicle. *Appl. Energy* **2020**, *260*, 114254–114265. [CrossRef]

39. de la Torre, S.; Sanchez-Racero, A.J.; Aguado, J.A.; Reyes, M.; Martianez, O. Optimal Sizing of Energy Storage for Regenerative Braking in Electric Railway Systems. *IEEE Trans. Power Syst.* **2015**, *30*, 1492–1500. [CrossRef]

40. Aguado, J.A.; Racero, A.J.S.; de la Torre, S. Optimal Operation of Electric Railways with Renewable Energy and Electric Storage Systems. *IEEE Trans. Smart Grid* **2018**, *9*, 993–1001. [CrossRef]

41. Torreglosa, J.P.; García-Triviño, P.; Fernández, L.M.; Jurado, F. Predictive Control for the Energy Management of a Fuel-Cell–Battery–Supercapacitor Tramway. *IEEE Trans. Ind. Inform.* **2014**, *10*, 276–285. [CrossRef]

42. Ceraoloa, M.; Lutzembergera, G.; Melib, E.; Pugib, L.; Rindib, A.; Pancaric, G. Energy storage systems to exploit regenerative braking in DC railway systems: Different approaches to improve ef fi ciency of modern high-speed trains. *J. Energy Storage* **2018**, *16*, 269–279. [CrossRef]

43. Moura, S.J.; Stein, J.L.; Fathy, H.K. Battery-Health Conscious Power Management in Plug-In Hybrid Electric Vehicles via Electrochemical Modeling and Stochastic Control. *IEEE Trans. Control Syst. Technol.* **2013**, *21*, 679–694. [CrossRef]

44. González-Gil, A.; Palacin, R.; Batty, P.; Powell, J.P. A systems approach to reduce urban rail energy consumption. *Energy Convers. Manag.* **2014**, *80*, 509–524. [CrossRef]

45. Zhang, B.; Mo, S.; Zhou, H.; Qin, T.; Zhong, Y. Finite-Time Consensus Tracking Control for Speed Sensorless Multi-Motor Systems. *Appl. Sci.* **2022**, *12*, 5518. [CrossRef]

46. Mejdoubi, A.E.; Oukaour, A.; Chaoui, H.; Gualous, H.; Sabor, J.; Slamani, Y. State-of-Charge and State-of-Health Lithium-Ion Batteries' Diagnosis According to Surface Temperature Variation. *IEEE Trans. Ind. Electron.* **2016**, *63*, 2391–2402. [CrossRef]

47. Zheng, Y.; He, Y.; Qian, K.; Li, B.; Wang, X.; Li, J.; Chiang, S.W.; Miao, C.; Kang, F.; Zhang, J. Deterioration of lithium iron phosphate/graphite power batteries under high-rate discharge cycling. *Electrochim. Acta* **2015**, *176*, 270–279. [CrossRef]

48. Wei, J.; Dong, G.; Chen, Z. Remaining Useful Life Prediction and State of Health Diagnosis for Lithium-Ion Batteries Using Particle Filter and Support Vector Regression. *IEEE Trans. Ind. Electron.* **2018**, *65*, 5634–5643. [CrossRef]

49. Chaoui, H.; Golbon, N.; Hmouz, I.; Souissi, R.; Tahar, S. Lyapunov-Based Adaptive State of Charge and State of Health Estimation for Lithium-Ion Batteries. *IEEE Trans. Ind. Electron.* **2015**, *62*, 1610–1618. [CrossRef]

50. García-Triviño, P.; Torreglosa, J.P.; Fernández, L.M.; Jurado, F. Control strategies for high-power electric vehicles powered by hydrogen fuel cell, battery and supercapacitor. *Expert Syst. Appl.* **2013**, *40*, 4791–4804. [CrossRef]